



## Mid-infrared detection of large longitudinal asymmetries in Io's SO<sub>2</sub> atmosphere

John R. Spencer<sup>a,\*</sup>, Emmanuel Lellouch<sup>b</sup>, Matthew J. Richter<sup>c,1</sup>, Miguel A. López-Valverde<sup>d</sup>,  
Kandis Lea Jessup<sup>a,1</sup>, Thomas K. Greathouse<sup>e,1</sup>, Jean-Marie Flaud<sup>f</sup>

<sup>a</sup> Department of Space Studies, Southwest Research Institute, 1150 Walnut St., Suite 400, Boulder, CO 80302, USA

<sup>b</sup> Observatoire de Meudon, DESPA, Meudon F-92195, France

<sup>c</sup> Department of Physics, University of California at Davis, One Shields Ave., Davis, CA 95616, USA

<sup>d</sup> Departamento Sistema Solar, Instituto Astrofísica de Andalucía, Apdo. 3004, 18080 Granada, Spain

<sup>e</sup> Lunar and Planetary Institute, 3600 Bay Area Blvd., Houston, TX 77058-1113, USA

<sup>f</sup> CNRS/University Paris-Sud, Lab. de Photophysique Moléculaire Campus d'Orsay, Bat. 350, F-91605 Orsay cedex, France

Received 26 July 2004; revised 13 January 2005

Available online 19 April 2005

### Abstract

We have observed about 16 absorption lines of the  $\nu_2$  SO<sub>2</sub> vibrational band on Io, in disk-integrated 19- $\mu\text{m}$  spectra taken with the TEXES high spectral resolution mid-infrared spectrograph at the NASA Infrared Telescope Facility in November 2001, December 2002, and January 2004. These are the first ground-based infrared observations of Io's sunlit atmosphere, and provide a new window on the atmosphere that allows better longitudinal and temporal monitoring than previous techniques. Dramatic variations in band strength with longitude are seen that are stable over at least a 2 year period. The depth of the strongest feature, a blend of lines centered at  $530.42\text{ cm}^{-1}$ , varies from about 7% near longitude  $180^\circ$  to about 1% near longitude  $315^\circ$  W, as measured at a spectral resolution of 57,000. Interpretation of the spectra requires modeling of surface temperatures and atmospheric density across Io's disk, and the variation in non-LTE  $\nu_2$  vibrational temperature with altitude, and depends on the assumed atmospheric and surface temperature structure. About half of Io's 19- $\mu\text{m}$  radiation comes from the Sun-heated surface, and half from volcanic hot spots with temperatures primarily between 150 and 200 K, which occupy about 8% of the surface. The observations are thus weighted towards the atmosphere over these low-temperature hot spots. If we assume that the atmosphere over the hot spots is representative of the atmosphere elsewhere, and that the atmospheric density is a function of latitude, the most plausible interpretation of the data is that the equatorial atmospheric column density varies from about  $1.5 \times 10^{17}\text{ cm}^{-2}$  near longitude  $180^\circ$  W to about  $1.5 \times 10^{16}\text{ cm}^{-2}$  near longitude  $300^\circ$  W, roughly consistent with HST UV spectroscopy and Lyman- $\alpha$  imaging. The inferred atmospheric kinetic temperature is less than about 150 K, at least on the anti-Jupiter hemisphere where the bands are strongest, somewhat colder than inferred from HST UV spectroscopy and millimeter-wavelength spectroscopy. This longitudinal variability in atmospheric density correlates with the longitudinal variability in the abundance of optically thick, near-UV bright SO<sub>2</sub> frost. However it is not clear whether the correlation results from volcanic control (regions of large frost abundance result from greater condensation of atmospheric gases supported by more vigorous volcanic activity in these regions) or sublimation control (regions of large frost abundance produce a more extensive atmosphere due to more extensive sublimation). Comparison of data taken in 2001, 2002, and 2004 shows that with the possible exception of longitudes near  $180^\circ$  W between 2001 and 2002, Io's atmospheric density does not appear to decrease as Io recedes from the Sun, as would be expected if the atmosphere were supported by the sublimation of surface frost, suggesting that the atmosphere is dominantly supported by direct volcanic supply rather than by frost sublimation. However, other evidence such as the smooth variation in atmospheric abundance with latitude, and atmospheric changes during eclipse, suggest that sublimation support is more important than volcanic support, leaving the question of the dominant atmospheric support mechanism still unresolved.

\* Corresponding author. Fax: +1 (303) 546 9687. Previously at: Lowell Observatory, 1400 W. Mars Hill Rd., Flagstaff, AZ 86001, USA.

E-mail addresses: [spencer@boulder.swri.edu](mailto:spencer@boulder.swri.edu), [mayo@mail630.gsfc.nasa.gov](mailto:mayo@mail630.gsfc.nasa.gov) (J.R. Spencer).

<sup>1</sup> Visiting Astronomers at the Infrared Telescope Facility, which is operated by the University of Hawaii under Cooperative Agreement no. NCC 5-538 with the National Aeronautics and Space Administration, Office of Space Science, Planetary Astronomy Program.

© 2005 Elsevier Inc. All rights reserved.

**Keywords:** Io; Atmospheres, Structure; Infrared observations; Radiative transfer; Spectroscopy

## 1. Introduction

Io's atmosphere is one of the most unusual and interesting in the Solar System, due to its unique composition (dominantly SO<sub>2</sub>) and unique structure. There are large lateral variations in density which are thought to result from rapid condensation of the dominant SO<sub>2</sub> gas away from volcanic or sublimation sources. The atmosphere thus offers unique insights into basic atmospheric physics. It is also the medium through which Io supplies the mass of the complex plasma that fills the jovian magnetosphere, and thus must be understood if we are to understand the jovian magnetospheric plasma. Recent reviews on Io's atmosphere and its interaction with the plasma torus can be found in McGrath et al. (2004) and Saur et al. (2004).

The atmosphere appears to cover most of the surface at low latitudes but is much thinner at high latitudes, as revealed most directly by imaging in reflected Lyman- $\alpha$  by the Hubble Space Telescope (HST). A subsolar SO<sub>2</sub> column density of a few  $\times 10^{16}$  cm<sup>-2</sup> has been inferred from the Lyman- $\alpha$  images (Feldman et al., 2000; Feaga et al., 2004). HST disk-integrated observations of 0.20–0.23  $\mu$ m SO<sub>2</sub> gas absorption bands give subsolar densities of a few  $\times 10^{16}$  cm<sup>-2</sup> (Ballester et al., 1994; Jessup et al., 2002) to  $\sim 10^{17}$  cm<sup>-2</sup> (Trafton et al., 1996) if the atmosphere is assumed to be concentrated over a few tens of percent of the surface at low latitudes, as suggested by the Lyman- $\alpha$  images. Disk-resolved 0.20–0.23  $\mu$ m spectroscopy away from plume sources gives low-latitude SO<sub>2</sub> densities of  $1.5 \times 10^{16}$  cm<sup>-2</sup> at longitude 318° W (McGrath et al., 2000) and  $1.3 \times 10^{17}$  cm<sup>-2</sup> at 160° W (Jessup et al., 2004). High column densities up to  $10^{19}$  cm<sup>-2</sup> have been inferred from Galileo UVS data (Hendrix et al., 1999), but are dependent on assumptions about the surface albedo, as UVS did not resolve individual SO<sub>2</sub> gaseous absorption bands.

SO<sub>2</sub> column density appears to be modestly enhanced over at least some volcanos. Voyager IRIS observations of the  $\nu_3$  vibrational band at 7.4  $\mu$ m implied  $9 \times 10^{16}$  cm<sup>-2</sup>– $2 \times 10^{18}$  cm<sup>-2</sup> of SO<sub>2</sub> at Loki (Pearl et al., 1979; reinterpreted by Lellouch et al., 1992), and UV absorption over Pele implied an SO<sub>2</sub> abundance of  $3 \times 10^{16}$  cm<sup>-2</sup> (McGrath et al., 2000) and  $7 \times 10^{16}$  cm<sup>-2</sup> (Spencer et al., 2000a), while abundance over Prometheus reached  $1.8 \times 10^{17}$  cm<sup>-2</sup> (Jessup et al., 2004). Disk-integrated mm-wave observations of SO<sub>2</sub> emission lines require local concentrations of a few  $\times 10^{17}$  cm<sup>-2</sup> of SO<sub>2</sub> at temperatures  $>600$  K to match observed line widths, if the atmosphere is static (Lellouch et al., 1992): such high temperatures are difficult to explain (Strobel et al., 1994). Lower temperatures, and local abundances of about  $1 \times 10^{17}$  cm<sup>-2</sup>, more consistent with the UV results, are possible if mm line widths

are due to rapid motions associated with plumes or supersonic winds (Ballester et al., 1994; Lellouch, 1996). In addition to SO<sub>2</sub>, lesser amounts of SO (Lellouch et al., 1996; McGrath et al., 2000), NaCl (Lellouch et al., 2003) and S<sub>2</sub> (Spencer et al., 2000a) have also been detected, as have neutral atomic emissions from S, O, and Na (Ballester et al., 1987; Geissler et al., 1999a, 2001a, 2004; Wolven et al., 2001; Feaga et al., 2004; Roesler et al., 1999; Bouchez et al., 2000), and molecular emissions from SO (dePater et al., 2002) and, probably, SO<sub>2</sub> and/or S<sub>2</sub> (Geissler et al., 1999a, 2001a, 2004; Jessup et al., 2004). The emission data are more difficult to interpret in terms of bulk atmospheric properties than the absorption data, as emission strength depends on excitation and dissociation mechanisms as well as atomic or molecular abundances.

SO<sub>2</sub> gas appears to be released by the volcanos either from primary vents (Spencer et al., 2000a) or from interaction of lava with surface frosts (Milazzo et al., 2001), condensing on the surface to form the extensive deposits of SO<sub>2</sub> frost seen on Io (Douté et al., 2001). The atmosphere is supported by a combination of direct volcanic supply and frost sublimation (Fanale et al., 1982; Ingersoll, 1989; Moreno et al., 1991; Wong and Smyth, 2000; Zhang et al., 2003). The relative roles of the volcanos and the surface frost in directly supporting the atmosphere depend on the frost temperature and the volcanic supply rate, and have not yet been determined. The arguments for the dominance of one or the other mechanism are considered later, in the discussion section. The question is important because a sublimation-supported atmosphere is likely to collapse at night and during Jupiter eclipse due to frost cooling, dramatically changing the interaction of Io with the magnetosphere (Wong and Smyth, 2000), and will have a different local distribution, being concentrated more around SO<sub>2</sub> frost deposits than active volcanic plumes.

Studies have been hampered by the difficulty in observing Io's atmosphere. While the first SO<sub>2</sub> detection (Pearl et al., 1979) was at 7.4  $\mu$ m, all subsequent observations of the sunlit molecular atmosphere (till now) have been in the Lyman- $\alpha$  and 0.2–0.3- $\mu$ m regions of the ultraviolet, where the HST is required, or at mm wavelengths, requiring large telescopes such as IRAM and CSO that have little time available for planetary studies. 1.7- $\mu$ m molecular SO emission is visible from the ground during Jupiter eclipse, perhaps due to direct volcanic emission of excited SO (dePater et al., 2002), but is difficult to relate to the bulk atmosphere. Full characterization of the atmosphere's temporal and spatial variability has thus been difficult.

Here we describe and interpret the first ground-based detection of Io's sunlit SO<sub>2</sub> atmosphere in the infrared. These observations open a new window for the study of Io's unique

atmosphere, and provide surprising new information on its temporal and spatial variability.

## 2. Observations and data reduction

We used the high-resolution mid-infrared Echelle spectrograph TEXES (the Texas Echelon-cross-Echelle Spectrograph, Lacy et al., 2001) at the 3.0-m NASA Infrared Telescope Facility (IRTF) on Mauna Kea in November 2001, December 2002, and January 2004 (Table 1). The observations described here concentrated on the wavenumber range 529–531  $\text{cm}^{-1}$  (18.90–18.83  $\mu\text{m}$ ) that includes several of the strongest lines in the  $\nu_2$  vibration/rotation band of  $\text{SO}_2$ , in a portion of the 20- $\mu\text{m}$  atmospheric window that is relatively free of telluric absorption bands. TEXES can observe only 3 or 4 cross-dispersed orders simultaneously at these wavenumbers, with small gaps in wavelength coverage between them. The exact grating setting, and wavelength range, varied between runs. We also experimented with observations at shorter wavelengths, including a portion of the  $\text{SO}_2$   $\nu_3$  band at 7.4  $\mu\text{m}$  that was seen by Voyager, where Io is much fainter and telluric obscuration is much greater (making observations possible only during periods of low telluric  $\text{H}_2\text{O}$  column abundance). No  $\text{SO}_2$  lines were seen in the 7.4- $\mu\text{m}$  region and these data will not be discussed further here.

In all cases, TEXES was used in its high resolution mode with a 2'' wide slit. Io was nodded, typically 5 or 6'', along the slit, and the spectra at the two nod positions were differenced to remove telescope and sky background emission. We observed an ambient temperature blackbody, sky, and a low emissivity surface roughly every 10 min to provide calibration data. Most data were taken at an airmass less than 1.2, and included some daytime observations. We also observed Callisto as a comparison object, as it is about 5 times brighter than Io at this wavelength. See Table 1 for details.

The data from Io and Callisto were reduced in the same way using the TEXES pipeline described in Lacy et al. (2001). The pipeline corrects for spikes and cosmic rays, removes background emission, removes distortions, and rectifies the 2D spectra. It uses optimal weighting to extract 1D spectra and sums spectra from the same observation set according to the square of the signal-to-noise.

The wavelength scale was set using a single atmospheric feature in the spectral setting, most often the 530.4089  $\text{cm}^{-1}$  feature of  $\text{CO}_2$  (we use vacuum wavenumbers throughout). Before taking data, we made certain of the wavelength setting by adjusting the cross-dispersion grating to see nearby, strong, easily identifiable atmospheric emission features of  $\text{H}_2\text{O}$ . Because the spectral orders are larger than the detector array at this wavelength, we adjusted the collimator/camera mirror to put the desired spectral region on the

Table 1  
Log of observations and band depths

UT date (YYMMDD)	Io central longitude ( $^\circ$ W)	Radial velocity ( $\text{km s}^{-1}$ )	Io mean airmass	Callisto mean airmass	Heliocentric distance (AU)	Fitted 530.42 $\text{cm}^{-1}$ band depth
011115	163	-25.7	1.08	1.19	5.15	0.057 $\pm$ 0.009
011116	334	-13.3	1.16	1.26	5.15	-0.005 $\pm$ 0.003
011116	345	-16.2	1.03	1.12	5.15	0.011 $\pm$ 0.011
011116	14	-24.4	1.22	1.12	5.15	0.022 $\pm$ 0.005
011117	205	-12.8	1.04	1.01	5.15	0.073 $\pm$ 0.005
011117	215	-9.9	1.19	1.52	5.15	0.059 $\pm$ 0.009
011118	36	-30.0	1.00	1.01	5.16	0.030 $\pm$ 0.005
011118	50	-33.0	1.06	1.08	5.16	0.033 $\pm$ 0.004
021206	194	-19.9	1.01	1.02	5.29	0.052 $\pm$ 0.007
021206	210	-15.2	1.19	1.04	5.29	0.051 $\pm$ 0.006
021209	90	-40.8	1.05	1.01	5.29	0.035 $\pm$ 0.009
021209	93	-40.7	1.09	1.16	5.29	0.038 $\pm$ 0.004
021214	22	-28.6	1.02	1.06	5.30	0.024 $\pm$ 0.011
021214	30	-30.6	1.11	1.21	5.30	0.023 $\pm$ 0.013
021214	35	-32.0	1.22	1.21	5.30	0.033 $\pm$ 0.007
021214	43	-33.6	1.48	1.36	5.30	0.028 $\pm$ 0.010
021217	256	-4.6	1.03	1.05	5.30	0.035 $\pm$ 0.006
021217	280	-4.1	1.12	1.05	5.30	0.017 $\pm$ 0.014
021219	311	-7.7	1.00	1.00	5.30	0.016 $\pm$ 0.008
021219	317	-8.9	1.02	1.06	5.30	0.007 $\pm$ 0.005
021219	319	-9.4	1.05	1.06	5.30	0.020 $\pm$ 0.006
021219	323	-10.1	1.08	1.13	5.30	0.008 $\pm$ 0.004
040106	98	-41.8	1.04	1.05	5.40	0.038 $\pm$ 0.003
040106	105	-41.3	1.04	1.04	5.40	0.044 $\pm$ 0.005
040107	301	-9.6	1.04	1.05	5.40	0.010 $\pm$ 0.005
040107	310	-11.1	1.05	1.06	5.40	0.011 $\pm$ 0.004
040108	140	-35.4	1.06	1.07	5.40	0.043 $\pm$ 0.002
040108	150	-32.7	1.04	1.05	5.40	0.054 $\pm$ 0.007

detector. This was also done by watching atmospheric emission lines and knowing where they should land on the detector. We estimate wavelength calibration accuracy to be  $0.002 \text{ cm}^{-1}$ , or  $1.0 \text{ km s}^{-1}$ . We averaged individual spectra to provide several mean spectra per night, excluding from the analysis any spectra with obvious guiding problems or cloud obscuration. We ratioed the  $19\text{-}\mu\text{m}$  Io spectra to Callisto spectra taken at similar airmass (generally within 0.1 airmasses), to remove telluric bands and variations in grating efficiency across each order, though continuum slope artifacts, which differ between spectrograph orders, remain in some cases. We then corrected wavelengths to Io's rest frame by applying the appropriate Doppler shift. The previously mentioned  $530.4089 \text{ cm}^{-1}$  telluric line often falls within the strongest  $\text{SO}_2$  band on Io, depending on the Doppler shift, but does not produce obvious artifacts in the ratio spectra due to the generally good airmass match between Io and Callisto, and we do not be-

lieve this feature compromises our measurements of the  $\text{SO}_2$  lines.

The final coadded and ratioed spectra have a signal-to-noise ratio of up to several hundred and a typical spectral resolution of  $65,000$  (Fig. 1). At least 16 lines of the  $\text{SO}_2 \nu_2$  band are readily apparent. We found that line positions differed significantly from those predicted by the HITRAN database of high-resolution molecular transmission spectra (Rothman et al., 1987, 2003), but were in agreement with more recent data, as discussed in Appendix A. Band strength varies significantly with longitude, with bands being strongest on the anti-Jupiter hemisphere (central longitude  $180^\circ \text{ W}$ ). The lines are unresolved, providing an upper limit to their intrinsic width equal to the TEXES spectral resolution at this wavelength,  $0.01 \text{ cm}^{-1}$  ( $5 \text{ km s}^{-1}$ ). These lines were not seen in the Voyager IRIS spectra of Io due to the much lower IRIS spectral resolution of  $4.3 \text{ cm}^{-1}$ .

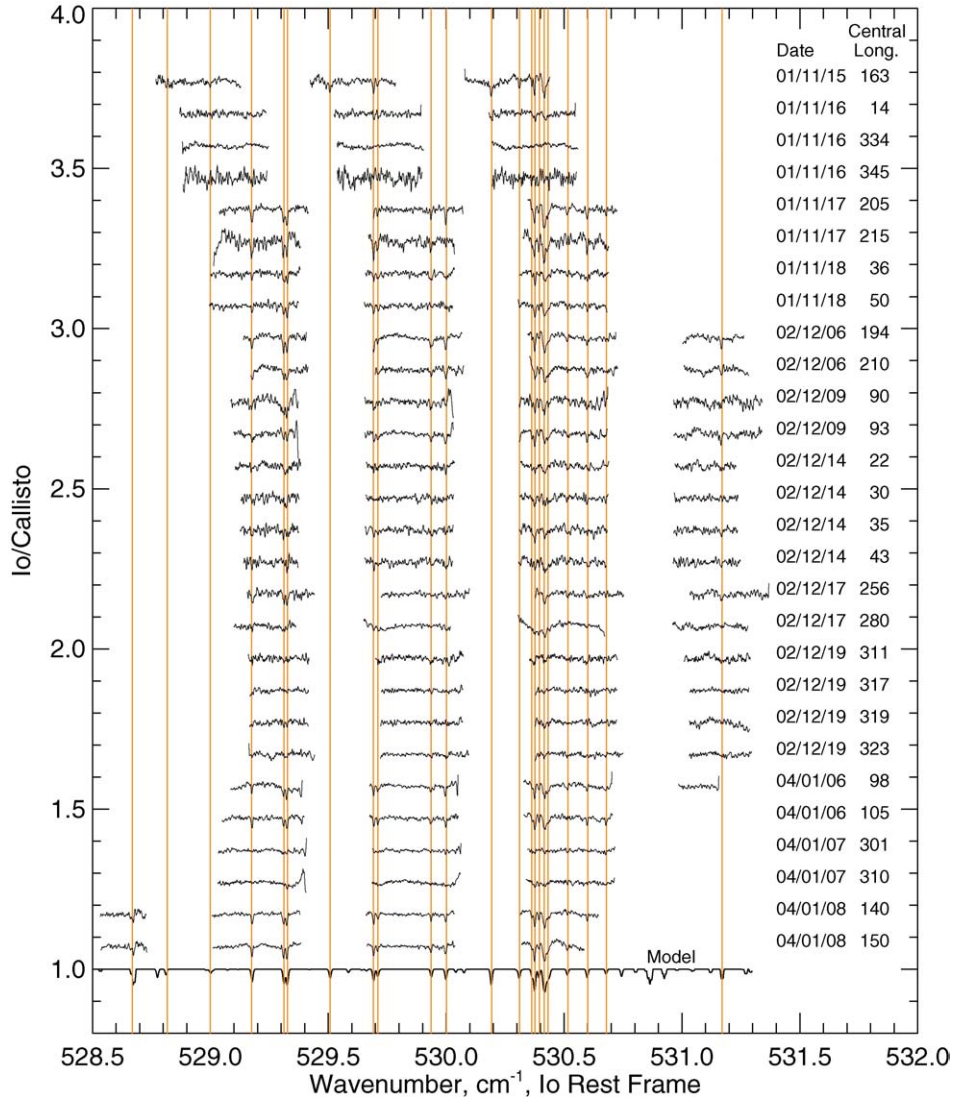


Fig. 1. Composite of all our Io spectra, with telluric and instrumental features removed by rationing to Callisto. The locations of  $\text{SO}_2$  bands seen in the model spectrum (bottom) are shown in orange: all of these are seen in at least some of the spectra. Successive spectra are offset vertically by 0.1.

### 3. Interpretation and modeling

In the thermal infrared, Io's atmosphere is illuminated from below by thermal emission from the passively-heated sunlit surface and from the volcanos. SO<sub>2</sub> vibration/rotation lines will be seen in emission if the vibrational temperature for the  $\nu_2 = 1$  state is greater than the underlying surface temperature, and will appear in absorption (as observed) if the surface is warmer than the vibrational temperature. However, at the low density of Io's atmosphere, collisional timescales are longer than radiative timescales, and vibrational temperatures are influenced by radiative exchange with the surface and deep space and cannot be assumed to be in local thermodynamic equilibrium (LTE) with the kinetic temperature of the atmosphere (Lellouch et al., 1992). The spectrum depends on the distribution of the atmospheric kinetic and vibrational temperatures, the atmospheric density, and the surface temperature, and we now describe how these various quantities are modeled and constrained.

#### 3.1. Non-LTE vibrational temperature models

A specific non-LTE model has been developed to calculate the population of the first excited state of SO<sub>2</sub> in its  $\nu_2$  mode of vibration, the (010) state, responsible for the 19- $\mu\text{m}$  absorption band. The model was also applied to the first excited states of the other two modes of vibration and to the  $\nu_1 + \nu_3$  state, and is able to produce both state populations and heating/cooling rates in the associated vibration-rotation bands. Here we only report on the results of occupation number of the (010) state.

The statistical equilibrium equation of the (010) state, including its most important production and loss processes, both collisional and radiative, was solved simultaneously with the radiative transfer equation of the fundamental band at 19  $\mu\text{m}$ . The solution method follows a modified Curtis Matrix formalism extensively employed in non-LTE problems in the upper atmosphere of Earth (López-Puertas and Taylor, 2001), Mars (López-Valverde and López-Puertas, 1994) and Venus (Roldán et al., 2000). In our case, given the absence of hot transitions and relevant vibrational-vibrational collisional exchanges with other excited states, the non-linearities of the problem are of very small importance, and the final solution is obtained with a single matrix inversion. An iteration was tested, however, after improving terms like the vibration partition function, with completely negligible effects on the results.

The radiative processes considered are the spontaneous and stimulated emission in the (010-000) fundamental band, the absorption of the upward thermal flux from the surface of Io, as well as exchanges between layers. The atmospheric transmittances required in the radiative model were computed following a histogram procedure which collects the different SO<sub>2</sub> lines in boxes according to their strength and then integrates the equivalent width of the representative line of each box with high spectral accuracy assuming a Voigt

profile. This “line-independent” approach assumes no important overlapping between SO<sub>2</sub> lines, and is justified given the low atmospheric densities and the spectral separation between the strongest lines in the  $\nu_2$  fundamental band. A similar approach has been found to be valid for the  $\nu_2$  mode of vibration of CO<sub>2</sub> in the martian atmosphere above about 50 km, or pressures lower than 30  $\mu\text{bar}$  (López-Valverde et al., 1998). A single collisional process is considered for the (010) state, its vibration-to-translation (V-T) relaxation in collisions with SO<sub>2</sub>, with a rate coefficient following Bass et al. (1971). The inverse V-T production is also considered, although its importance is small compared to radiative excitation in most conditions, as explained below.

The model is run from the surface up to 200 km, with 1-km thick layers, assuming that all the atmosphere is composed of SO<sub>2</sub>. The spectral data are taken from the HITRAN database. The 0.12-cm<sup>-1</sup> wavelength errors in the HITRAN database noted in Appendix A are unimportant to this calculation, given the line-independent assumption mentioned above.

A few other approximations are used, like rotational LTE at all altitudes. We think that a complete non-LTE treatment of the rotational distribution within the SO<sub>2</sub> band is an unnecessary complication in the lower parts of Io's atmosphere. High quality laboratory information is not available for collisional activation of rotational lines, and also our observations do not have a signal-to-noise ratio large enough to test more detailed models. Also, although the LTE assumption for the rotational lines is not very accurate for the uppermost layers considered here, the 19- $\mu\text{m}$  fundamental band is optically thin above about 2 scale heights (around 20–30 km), and at lower altitudes, where the spectral features are mostly formed, the atmospheric density is high enough ( $\sim 1$  nbar) for this assumption to be reasonable.

This non-LTE model assumes a given atmospheric state. To model the data for a range of surface and atmospheric conditions, we performed a number of runs varying surface temperature, column density, and atmospheric pressure, and typical results are shown in Fig. 2, with the corresponding spectra, calculated as described in the next section, shown in Fig. 3. Here we illustrate the (010) state population as a function of altitude using the concept of vibrational temperature,  $T_V$ . This is a useful parameter in non-LTE studies because it matches the atmospheric kinetic temperature,  $T_K$ , if in LTE, while  $T_V < T_K$  when the state is underpopulated due to an important loss mechanism, like emission to space.  $T_V$  is shown in Fig. 2 for a number of conditions which illustrate the behavior of the model.

In the left panel,  $T_V$  is shown for an isothermal atmosphere at 100 K, and for two values of the SO<sub>2</sub> column amount,  $9 \times 10^{16}$  and  $9 \times 10^{17}$  cm<sup>-2</sup> (curves A and B, respectively). The surface temperature is set equal to the atmospheric temperature. In the denser atmosphere,  $T_V$  matches  $T_K$  in the lowest layers, i.e., it is in LTE near the ground, and it tends to values lower than  $T_K$  higher up. This is a very common behavior in many non-LTE problems, with

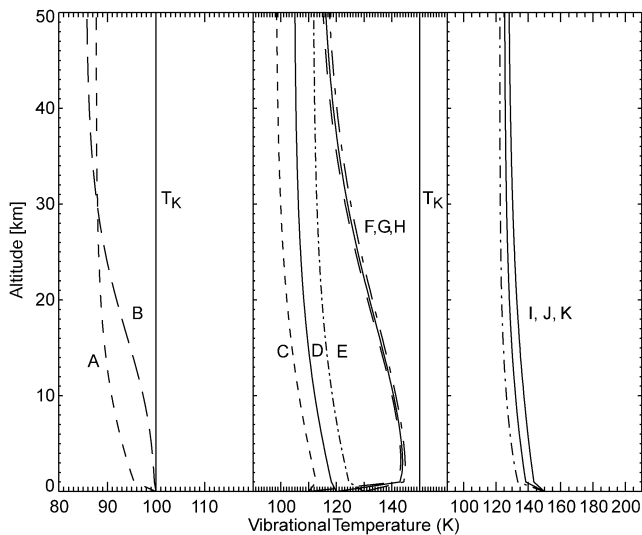


Fig. 2. Vibrational temperature of the  $\text{SO}_2$   $\nu_2$  fundamental band for a number of cases. Left panel: for an isothermal atmosphere at 100 K, surface temperature of 100 K, and column densities of  $\text{SO}_2$  of  $9 \times 10^{16}$  (A) and  $9 \times 10^{17} \text{ cm}^{-2}$  (B). Central panel: for an isothermal atmosphere at 150 K and surface temperatures of 110 (dashed: (C) and (F)), 120 (solid: (D) and (G)) and 130 K (dot-dash, (E) and (H)), and for column densities of  $9 \times 10^{16}$  (thick) and  $9 \times 10^{17} \text{ cm}^{-2}$  (thin). Right panel: for an atmosphere with a column density of  $9 \times 10^{16} \text{ molecule cm}^{-2}$  and a fixed surface temperature of 150 K, and kinetic temperatures of 100 (I), 150 (J) and 200 K (K).

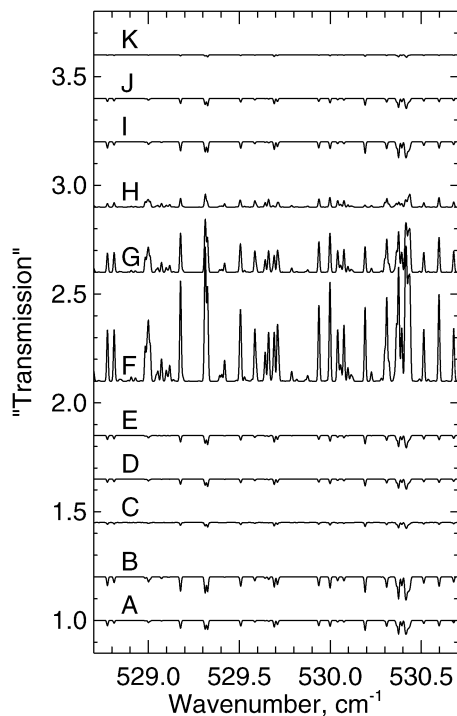


Fig. 3. Model spectra corresponding to the atmospheric vibrational temperature profiles shown in Fig. 2. Successive spectra are offset vertically, for clarity.

collisions dominating over radiative losses in the lowest altitudes. At lower densities (curve A), collisions are less important and the departure from LTE is larger. Above 30 km,

in contrast,  $T_V$  is larger in the less dense atmosphere, due to the reduced absorption of the upward thermal flux from the surface. Notice that  $T_V$  in this example is lower than the surface temperature at all altitudes, resulting in an absorption spectrum since the  $\nu_2$  emission is controlled by  $T_V$ .

The central panel shows the importance of the surface upward flux.  $T_K$  is fixed at 150 K, while surface temperature is varied, but kept lower than the kinetic temperature, with values of 110, 120, and 130 K (curves C, D, E, and F, G, H). The upward surface flux is very important in the less dense atmosphere ( $9 \times 10^{16} \text{ cm}^{-2}$ , curves C, D, E), and not in the denser one ( $9 \times 10^{17} \text{ cm}^{-2}$ , curves F, G, H). In this last case,  $T_V$  is higher than the surface temperature, producing emission spectra.

Another interesting behavior is illustrated in the right panel, where the surface temperature and the column density are fixed at 150 K and  $9 \times 10^{16} \text{ cm}^{-2}$ , respectively, while changing  $T_K$  from 100 to 150–200 K (curves I, J, K, respectively). In spite of these large variations in  $T_K$ , the  $T_V$  profile is only slightly modified. This shows that for relatively low densities  $T_V$ , and thus the resulting spectrum, is largely controlled by radiative exchange between the surface and space and is little affected by  $T_K$ . For larger densities, the atmosphere becomes very optically thick and the other radiative term, the exchange between layers, becomes very important.

An increase in atmospheric density can therefore produce an increase in absorption strength (cf. curves A and B) or (if  $T_K$  is warmer than the surface and the atmosphere is sufficiently dense) a decrease in absorption strength, potentially producing emission lines, due to the increased vibrational temperature (cf. curves E and H). This leads to ambiguities in interpreting the mid-IR spectra, as discussed later.

Io's vertical atmospheric structure has been the subject of considerable modeling (see Strobel et al. (1994) and Wong and Smyth (2000) for the most recent works) but is observationally poorly constrained. Even the mean gas kinetic temperature remains uncertain, although recent HST and mm data tend to suggest low ( $<250$  K) temperatures (McGrath et al., 2000; Jessup et al., 2004; McGrath et al., 2004). For this reason and for simplicity, we only considered isothermal atmospheres. We calculated profiles of vibrational temperature with height for a range of surface temperatures (90, 100, 110, 120, 130, 140, 160, 180, 200, and 250 K); isothermal atmospheric kinetic temperatures (100, 125, 150, 175, 200, 225, 250, 275, and 300 K); and atmospheric column densities ( $1 \times 10^{16}$ ,  $2 \times 10^{16}$ ,  $3 \times 10^{16}$ ,  $6 \times 10^{16}$ ,  $1 \times 10^{17}$ ,  $2 \times 10^{17}$ ,  $3 \times 10^{17}$ ,  $6 \times 10^{17}$ , and  $1 \times 10^{18} \text{ cm}^{-2}$ ) as described above.

### 3.2. Calculation of spectra

Model atmospheres were then incorporated in a multi-layer, line-by-line radiative transfer code to calculate model spectra, using more recent  $\text{SO}_2$  line parameters than the HITRAN database, which we found to contain significant

wavelength errors (see Appendix A). The model is very similar to usual LTE calculations, with two differences. First, when calculating line strengths and monochromatic opacities at each atmospheric level, the vibrational temperature was used instead of the kinetic temperature to calculate the vibration partition function. Second, and most importantly, when calculating the Planck integral, the kinetic temperature was also replaced by the vibrational temperature, i.e., the local source function was taken as the Planck function at the local vibrational temperature. In some situations, this resulted in absorption lines even with a kinetic temperature higher than the surface temperature; this occurred when the bulk of the atmosphere had a vibrational temperature colder than the surface. An example is the case  $T_K = 150$  K,  $T_{\text{Surface}} = 120$  K, column density =  $9 \times 10^{16}$  cm<sup>-2</sup>, curve D in Figs. 2 and 3. Spectra for all model atmospheres were calculated for five values of the airmass (1.0, 1.5, 2.0, and 3.0, and 4.5), representing the range of viewing conditions at Io, giving a total of 4050 model spectra.

### 3.3. Surface temperature model

Several constraints on Io's surface temperature distribution are available. The most detailed existing model is that of Veeder et al. (1994), who matched multi-wavelength disk-integrated ground-based photometry of Io with a thermal model that included passive (non-volcanic) and volcanic components. Veeder et al. modeled the passive flux as arising from two components: a high-albedo "reservoir unit" assumed to have infinite thermal inertia and thus a temperature that depends only on latitude, comprising roughly 80% of the surface, plus a lower-albedo "conventional unit" with zero thermal inertia and thus a temperature depending only on distance from the subsolar point. Their model also represented the hundreds of volcanic hot spots with ten model hot spots with fixed locations distributed around Io, with temperatures and areas that were adjusted to fit each year's ground-based observations.

However, because atmospheric density and airmass both vary across Io's disk, to calculate the disk-integrated atmospheric spectrum we needed to adapt the model, originally designed to match disk-integrated fluxes only, to predict the distribution of temperatures at each point on the surface, so that the model correctly calculates the illumination of the atmosphere at each point. We divided the dayside hemisphere visible from Earth into tiles with 5° increments of latitude and local time, to account for variations in passive temperature and atmospheric parameters. To model volcanic flux, for a given sub-Earth longitude on Io we then determined from the Veeder et al. (1994) model the temperatures, projected areas, and fluxes of all visible model hot spots. Because (with the exception of the giant hot spot Loki) Io's mid-IR volcanic flux is in reality widely distributed in a large number of hot spots scattered across the disk (Spencer et al., 2000b; Rathbun et al., 2004), we assumed for simplicity

that this total volcanic flux was uniform across the disk, and distributed the flux from each visible hot spot, at the temperature of that hot spot, among all tiles according to their projected area. For each tile we also calculated the temperature and projected flux for the two model passive surface components, which we assumed, like the hot spots, to be spatially mixed on a scale smaller than our tiles. We implicitly assumed, however, that the different surfaces are segregated on scales larger than an atmospheric scale height (about 11 km), as our model spectra assume illumination by a uniform temperature surface. For each tile the model yielded two passive temperatures and several hot spot temperatures (depending on how many model hot spots were on Io's visible hemisphere for the chosen central longitude), and recorded the contribution to the disk-integrated 18.9- $\mu$ m flux from each temperature component.

Because the Veeder et al. model only modeled volcanic fluxes from Io for the years 1983–1993, and did not cover the period of our observations, we arbitrarily used the 1983 hot spot data from the anti-Jupiter hemisphere in our standard model. Calculated band depth did not vary much with assumptions about volcanic activity, with the largest effect being that band depth increased somewhat when Loki, Io's largest volcano, was on the disk (Figs. 9 and 16, discussed later).

We tested our thermal model in several ways. First, we compared the model to the best Galileo PPR map of daytime thermal emission on Io, the observation 31IPDGTM\_01 obtained at 27  $\mu$ m on Galileo's I31 encounter with Io (Rathbun et al., 2004; their Fig. 1). Fig. 4 compares this brightness temperature map to maps calculated from our thermal model. In its original form our model predicted too much flux near the limb and not enough near the subsolar point. The discrepancy is not surprising, as the model was designed to match disk-integrated flux only. We therefore improved the match to the data by introducing an empirical weighting factor that modified the temperature of each component so as to multiply the flux at each solar incidence angle  $i$  by the weighting factor  $0.97(0.3 + \cos(i))$ , which has a mean value of unity across Io's projected disk and thus preserves the known total flux. Fig. 4 shows that with the inclusion of this factor the Galileo observations are reproduced quite well.

We also compared a near-disk-integrated spectrum of Io observed by Voyager IRIS in 1979 to the spectrum predicted by our model (Fig. 5). This test is somewhat crude because the Voyager spectrum was obtained at a phase angle of 15 degrees while our model calculates only zero-phase emission, and the Voyager field of view did not exactly match Io's disk. However, the match is still quite good. The model underestimates 19- $\mu$ m flux by 12%, though the mismatch would be greater if the model were corrected to the phase angle of the observations.

Fig. 6 shows the cumulative distribution of disk-integrated 530-cm<sup>-1</sup> flux as a function of temperature for our standard surface thermal model. About half the disk-integrated flux

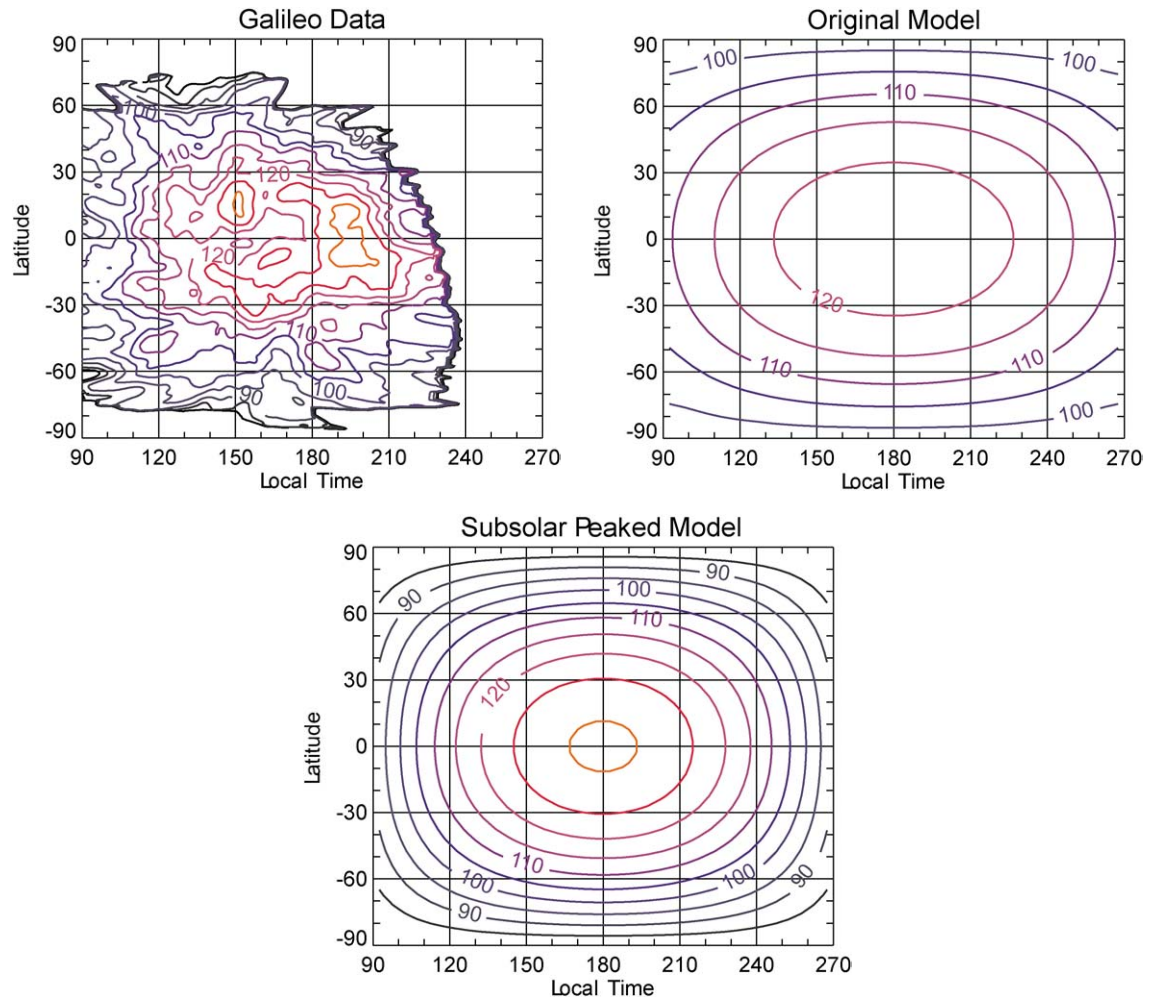


Fig. 4. Io's 27- $\mu\text{m}$  brightness temperature vs latitude as measured by the Galileo PPR instrument during its 31IPDGTM\_01 observation with a subsolar longitude of  $110^\circ$  W (Rathbun et al., 2004) compared to our thermal model, calculated at the same longitude and heliocentric distance. The upper right panel shows the original model, and the bottom panel shows our final model, after application of an empirical correction that boosts subsolar temperatures and suppresses near-terminator temperatures, as described in the text. The final model is a better match to the data.

comes from passive surfaces below 160 K, and half from volcanic hot spots in the 150–200 K range.

### 3.4. Atmosphere model

To determine disk-integrated line strengths as a function of atmospheric abundance, we considered four different models for Io's atmospheric distribution. In each case a range of peak frost temperatures is considered, each giving a peak  $\text{SO}_2$  column density assuming hydrostatic equilibrium and the vapor pressure formulation of Wagman (1979). Frost temperature, and consequent  $\text{SO}_2$  density, is scaled across the globe from the peak value according to various assumptions, as follows:

1. Globally-uniform. While there are numerous lines of evidence suggesting that the atmosphere is highly non-uniform, this model provides a useful end-member for comparison with more realistic models.
2. Solar incidence angle dependence. Frost temperature varies with solar incidence angle on the assumption of uniform albedo and zero thermal inertia. Atmospheric abundance then depends only on solar incidence angle, i.e., the distance from the subsolar point. This model is roughly consistent with recent disk-resolved HST 2000–3000 Å spectroscopy of Io (Jessup et al., 2004), as shown in Fig. 7, but is less consistent with HST Ly- $\alpha$  images of Io (Feldman et al., 2000; Feaga et al., 2004), which suggest that atmospheric density depends mostly on latitude. However, the Ly- $\alpha$  data do not rule out solar incidence dependence if Io's equatorial darkness at Ly- $\alpha$  wavelengths is due to low equatorial albedo in addition to gas absorption.
3. Latitude dependence: equilibrium with surface frost of uniform albedo and constant diurnal temperature, i.e., infinite thermal inertia. Atmospheric abundance then depends only on latitude. This model is also roughly consistent with the Jessup et al. (2004) observations

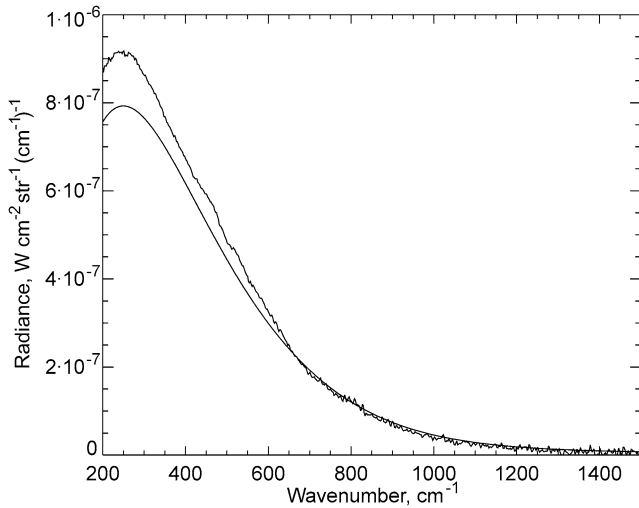


Fig. 5. Comparison of the full-disk thermal emission spectrum from Io as observed by Voyager IRIS (an average of FDS counts 16368.29–16368.31), to the predictions from our final thermal model run at the same central longitude and heliocentric distance. The match is quite good, despite the fact that no model parameters have been adjusted to fit this observation, suggesting that the model predicts the range of temperatures on Io with reasonable accuracy.

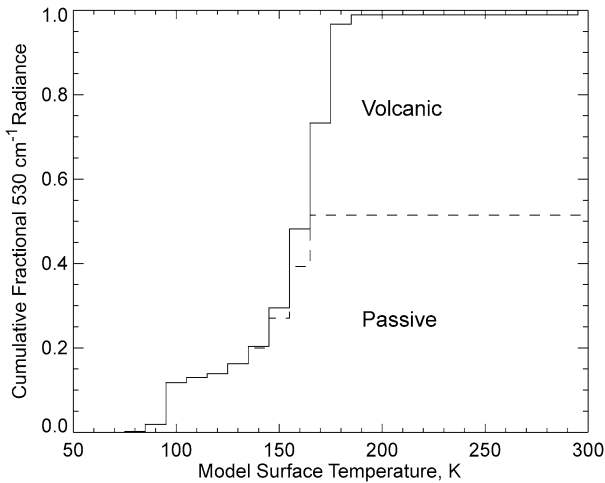
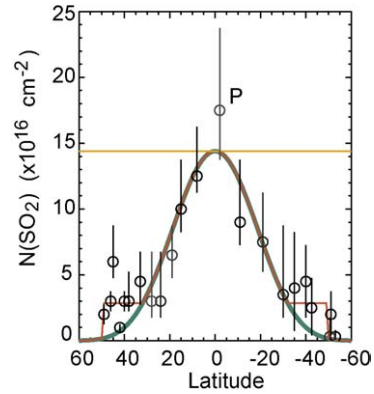


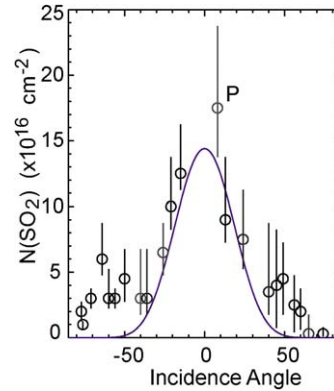
Fig. 6. The contribution to the total disk-integrated  $530\text{ cm}^{-1}$  radiance (solid line) from different temperatures in the standard version of our surface thermal model ( $R = 5.30\text{ AU}$ , longitude =  $180^\circ\text{ W}$ ). The cumulative passive contribution is below the dashed line, the volcanic contribution is above the dashed line. About half the radiance is from passive surface components colder than  $160\text{ K}$ , and half is from volcanic components in the  $150\text{--}200\text{ K}$  temperature range.

(Fig. 7), and is more consistent with the Ly- $\alpha$  images than model 2. Latitude dependence could also be consistent with an atmosphere supported by low-latitude volcanic activity (Strobel and Wolven, 2001).

4. Modified latitude dependence. Fig. 7 shows that the simple frost equilibrium models 2 and 3 above underestimate the observed  $\text{SO}_2$  gas abundance at mid-latitudes on Io. We therefore also tested a modified latitude dependence model, more consistent with the Jessup et al. observations, in which atmospheric abundance



(a)



(b)

Fig. 7. Comparison of model number density vs latitude (a) and solar incidence angle (b) to the observed limb-to-limb number density profile observed on Io's anti-jovian hemisphere from HST 2000–3000 Å spectroscopy (Jessup et al., 2004), for a subsolar number density of  $1.44 \times 10^{17}\text{ cm}^{-2}$ . The models are the uniform model (dark yellow); latitude dependence (green); modified latitude dependence (red) which provides the best match to the data; and incidence dependence (purple (b)). The observation that includes the Prometheus plume, which shows excess  $\text{SO}_2$ , is denoted by “P”

is in equilibrium with infinite thermal inertia surface frost at low latitudes, but is held constant at its latitude  $32^\circ$  value between absolute latitudes  $32^\circ$  and  $50^\circ$ . This model approximates the likely moderation of the abundance gradient with latitude due to hydrodynamic flow away from the equator (Wong and Johnson, 1996; Wong and Smyth, 2000; Austin and Goldstein, 2000), or accounts for additional volcanic support at mid-latitudes. A more gradual drop in  $\text{SO}_2$  abundance with latitude than expected for simple sublimation models was also seen by McGrath et al. (2000). Poleward of  $50^\circ$  latitude we return to the simple sublimation model, obtaining very low  $\text{SO}_2$  abundances generally consistent with the  $1 \times 10^{15}\text{ cm}^{-2}$  upper limit for the polar regions derived by Strobel and Wolven (2001).

Our standard model assumes an atmosphere that is smoothly distributed on regional scales, and is not concentrated over individual hot spots. This assumption is supported to some extent by disk-resolved HST spectroscopy (Jessup et al., 2004) and Lyman- $\alpha$  mapping (Feaga et al.,

2004), which show modest (at most) local concentrations of gas over most volcanic centers at HST’s 150–200 km resolution. But because about half of Io’s 19- $\mu\text{m}$  radiance probably comes from hot spots in the 150–200 K temperature range (Fig. 6), which cover a small fraction (about 8%) of the surface, our inferred column densities are weighted towards the atmosphere above hot spots, and may overestimate mean atmospheric densities if the gas is concentrated over these hot spots at scales smaller than can be resolved by HST, as discussed in the next section.

### 3.5. Disk-integrated model

We combined all the above elements to determine Io’s disk integrated mid-infrared spectrum, as illustrated in Fig. 8. We used the thermal model to determine the continuum flux contribution from each temperature component in each spatial tile on the illuminated disk, and used the atmospheric and spectroscopic models to determine each component’s contribution to the spectrum of the thermal emission, given the surface temperature, atmospheric kinetic temperature (assumed to be constant across Io’s disk), column abundance, and the airmass appropriate for each spatial tile. The assumption of globally-uniform kinetic temperature is necessary because of the lack of constraints on temperature variations from the available HST and mm data. We

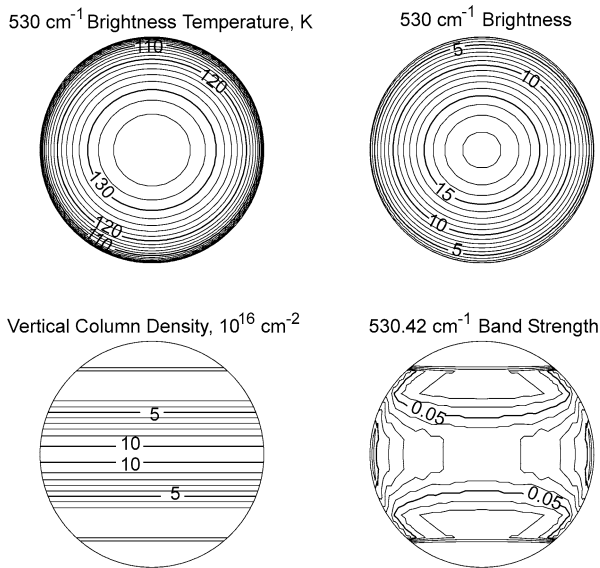


Fig. 8. Illustration of one of our disk-integrated thermal/atmospheric models, showing Io’s projected disk centered on the subsolar point, with north at the top. The top two panels show the surface brightness temperature and brightness (in units of  $10^{-6} \text{ W } \mu\text{m}^{-1} \text{ str}^{-1} \text{ cm}^{-2}$ ) that illuminates the atmosphere. The lower left panel shows the vertical column density, for the modified latitude model with subsolar column density  $1.03 \times 10^{17} \text{ cm}^{-2}$ . The lower right panel shows the model  $530.42 \text{ cm}^{-1}$  band depth, with contour increment 0.01, for an atmospheric kinetic temperature of 125 K. Band strength is highest near the equator where the atmosphere is thick and near the limb where the airmass is high. This spectrum distribution is weighted by the 18.9- $\mu\text{m}$  brightness (upper right) when calculating the disk-integrated spectrum.

used linear interpolation to obtain spectra for parameters intermediate to the 4050 parameter combinations that we previously calculated. For abundances less than the minimum model abundance,  $1 \times 10^{16} \text{ cm}^{-2}$ , we assumed that line strength varied linearly with abundance, justified by the almost linear relation between band strength and column abundance in the  $1 \times 10^{16}$ – $2 \times 10^{16} \text{ cm}^{-2}$  range in our models. The sum of all these spectral contributions gave the final disk-integrated spectrum. We determined the disk-integrated spectrum for each of our four models for peak (global, subsolar or equatorial) column abundances ranging from  $6 \times 10^{15}$  to  $1.3 \times 10^{18} \text{ cm}^{-2}$ .

We determined model spectrum band depths at a fixed spectral resolution approximating the TEXES instrumental resolution, by convolving with a Gaussian with a resolving power of 57,000 FWHM. Fig. 9 shows the depth, defined as (continuum flux–band center flux)/continuum flux, of the strongest band in our spectral range (at  $530.42 \text{ cm}^{-1}$ , actually a blend of several unresolved lines), for a range of atmospheric kinetic temperatures  $T_K$  and column densities, for our preferred “modified latitude” model with various model parameters adjusted to explore the sensitivity of the results to model assumptions. The upper left panel shows results from the model as described above. The upper right panel shows the negligible effect of replacing the two passive surface components in the Veeder et al. model with a single component at intermediate temperature radiating the same total flux, and suggests that our results are not very dependent on the details of the passive surface model. The lower left panel shows that except at the lowest kinetic temperatures, band strengths increase slightly when Loki, Io’s largest volcano, is on the observed hemisphere, due to Loki’s large flux contribution at high surface temperatures which produce stronger bands. The lower right panel shows that the increased surface temperatures associated with decreasing heliocentric distance from our nominal value of 5.30–5.10 AU (which increases passive surface temperatures by about 2%) have negligible effect on band strength. However, variations in the column density of a sublimation atmosphere with heliocentric distance, due to varying frost temperature, are not included in the model in Fig. 9 and could be significant, as discussed later. Despite the complexity of our thermal model, the band strengths that it predicts do not appear to be unduly model-dependent.

Fig. 10 shows band strengths for two extreme models in which the atmosphere is present only above the hot spots, and is absent elsewhere. The models assume either constant density above all hot spots or latitude-dependent density, simulating the observed equatorial concentration of volcanic plumes (McEwen and Soderblom, 1983). Band strengths in these models are within a factor of two of the band strengths in our standard model for the same column density if  $T_K$  is low, with larger variations at higher atmospheric temperatures. The regional average column density in these models is about  $12\times$  lower than the column density over the hot

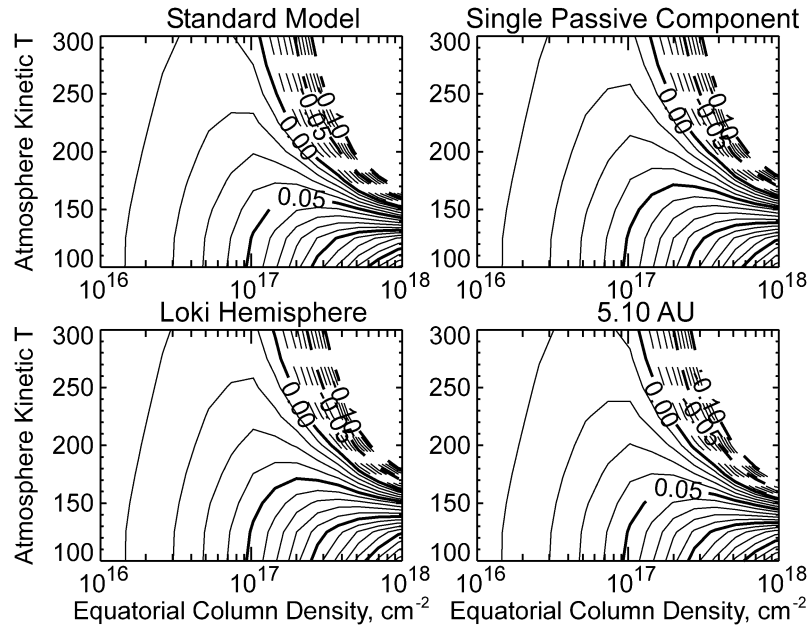


Fig. 9. Sensitivity of the depth of the strongest  $\text{SO}_2$  band in our wavelength range, at  $530.42 \text{ cm}^{-2}$ , as determined at our standard spectral resolution of 57,000, to various adjustable parameters in the Io thermal model. In each panel, only one parameter has been changed from the standard model ( $R = 5.30 \text{ AU}$ , longitude =  $180^\circ \text{ W}$ , 1983 hot spots, Veeder et al. (1994) passive surface temperature model, “modified latitude” atmospheric model). The model is relatively insensitive to changes in model parameters: for instance band depth for  $N = 2 \times 10^{17} \text{ cm}^{-2}$ ,  $T_K = 150 \text{ K}$  is 0.060 for the standard model, 0.065 if passive temperatures are locally isothermal, 0.065 for the different model distribution of volcanic and passive temperatures on the Loki hemisphere (central longitude =  $310^\circ \text{ W}$ ), and 0.061 if heliocentric distance is reduced to 5.10 AU. Dashed lines indicate negative band depth, i.e., emission spectra.

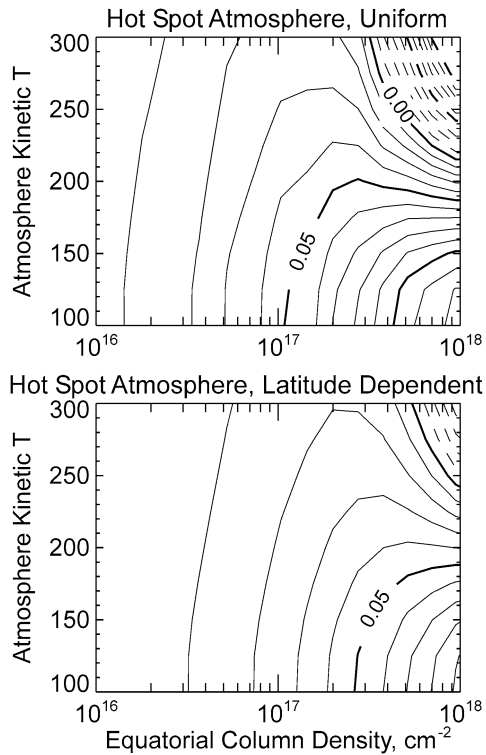


Fig. 10. Model  $530.42\text{-cm}^{-1}$  band depth, assuming the atmosphere is present only above volcanic hot spots. The top panel assumes that the hot spot atmosphere is independent of surface location, while the bottom panel assumes that the atmospheric abundance over the hot spots follows the modified-latitude model. The  $x$  axes describes the column density over the hot spots only. Other details as in Fig. 9.

spots that is shown in Fig. 10, because the hot spots in the Veeder et al. (1994) model cover only  $\sim 8\%$  of the surface.

Fig. 11 shows the band strength results from our standard surface thermal model, for all four atmosphere models (excluding the hot-spot-only models of Fig. 10). The trends in these models can be understood by remembering that band depth is controlled by the column abundance and the temperature contrast between the  $\text{SO}_2$  vibrational temperature  $T_V$  and the surface temperature, which has the same distribution in all these models. At low  $T_K$ ,  $T_V$  is colder than the mean surface temperature for all column densities, so lines are seen in absorption and their strength increases monotonically with column density. At low column densities the same is true for higher  $T_K$ , because at low densities  $T_V$  is controlled radiatively and is little affected by  $T_K$ , so  $T_V$  remains low and band strength is almost independent of  $T_K$ . However, as  $T_K$  or density increase,  $T_V$  also increases, causing line depths to decrease and finally producing emission features at sufficiently high  $T_K$  or column density, as seen in the upper right of the plots.

The uniform model produces the strongest lines for a given peak column density, because the disk-averaged column density is the highest, and conversely the incidence model produces the weakest lines because the atmospheric density falls off in all directions from the disk center. The two latitude-dependent models, where atmospheric density falls off only towards the poles, have intermediate band strengths, with slightly higher band depths in the modified latitude model due to the enhanced mid-latitude densities.

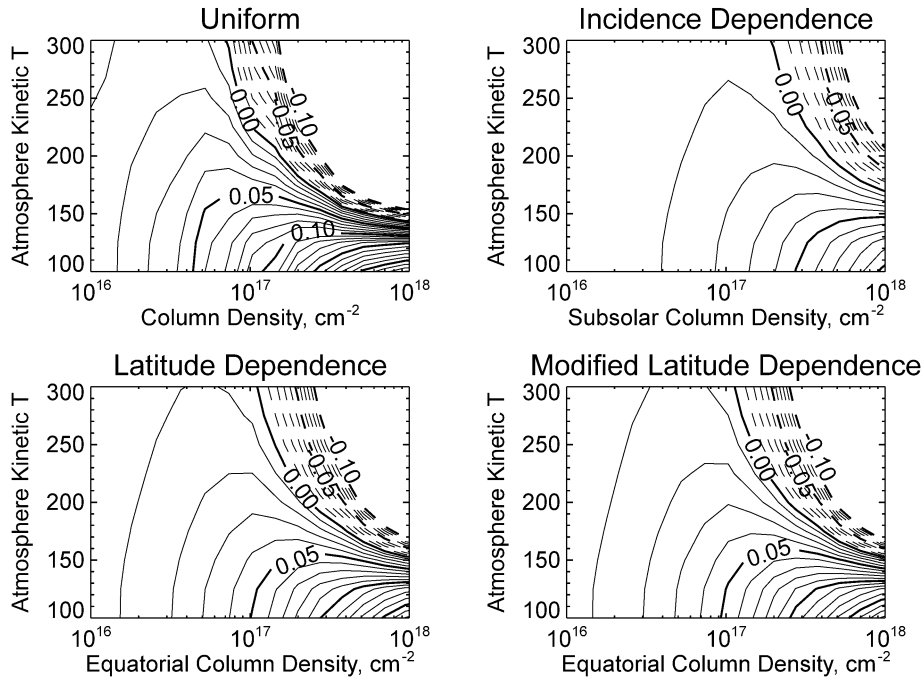


Fig. 11.  $530.42\text{-cm}^{-1}$  band depth for our four atmospheric models (excluding the hot-spot-only atmosphere models) with nominal conditions, for a range of peak column densities and atmospheric kinetic temperatures. Other details as in Fig. 9.

#### 4. Spectrum fitting

For this initial analysis we did not attempt to fit the detailed shape of each spectrum, but simply measured the observed  $530.42\text{-cm}^{-1}$  band strength and compared this to the strength of the same band derived from the models. We measured band strength by fitting the  $530.34\text{--}530.49$  region of each telescopic spectrum with a model template derived from a single arbitrarily-chosen model spectrum (surface temperature = 160 K,  $T_K = 125$  K, airmass = 1, and column abundance =  $1.0 \times 10^{17}$   $\text{cm}^{-2}$ ), linearly scaling the model absorption strength by the same factor at all wavelengths to fit the data. The use of linear scaling is justified by the weakness of the lines at the observed resolution, and the choice of template spectrum was not critical, because those model spectra that showed absorption rather than emission bands generally had similar band shapes in the region of interest, differing mostly in band strength. Figs. 12 and 13 justify these simplifications by showing that the model template fits the actual spectra in this spectral region very well, and provides an accurate measure of band depth. The model was calculated at a spectral resolution of 120,000, higher than that of any of our data, and convolved with a variable-width Gaussian to match the spectral resolution of the data. Using a Simplex technique, we adjusted the model band depth (measured at our standard spectral resolution of 57,000), continuum slope, spectral resolution, and wavelength (the latter within tightly proscribed limits consistent with our wavelength calibration) to obtain the best fit to each observed spectrum. We estimated uncertainties in band depth by a Monte Carlo technique, adding noise similar to

that in each spectrum to its best-fit model, and determining the standard deviation of the parameters obtained by multiple fits to the noisy model. Errors given here are twice this standard deviation and are thus formally two-sigma errors. The best fits are shown in Fig. 12, sorted by orbital longitude, and are tabulated in Table 1. Fig. 13 shows the fits to a few of the more interesting spectra in more detail, including uncertainties. Fig. 14 shows the variation in the strength of the  $530.42\text{-cm}^{-1}$  band with orbital longitude, and Fig. 15 shows the full spectra binned by longitude, compared to disk-integrated models with similar band strength. This figure shows that models which match the blended  $530.42\text{-cm}^{-1}$  lines also match the other lines adequately, because of the correlation in line strength between the bands. The line strength ratios of some line pairs (for instance the pair at  $529.323$  and  $529.307$   $\text{cm}^{-1}$ ) are temperature dependent in the models, and the observed ratios might provide additional model constraints with more detailed modeling, though S/N is poorer for the weaker lines.

#### 5. Discussion

##### 5.1. Overall spectrum shape

The most obvious characteristic of our spectra is that, with the possible exception of one spectrum at central longitude  $334^\circ$  W that shows possible very weak emission lines (Fig. 13), the  $\text{SO}_2$  lines are always seen in absorption. This is in contrast to the mm-wave region where  $\text{SO}_2$  lines are always seen in emission (Lellouch et al., 1992;

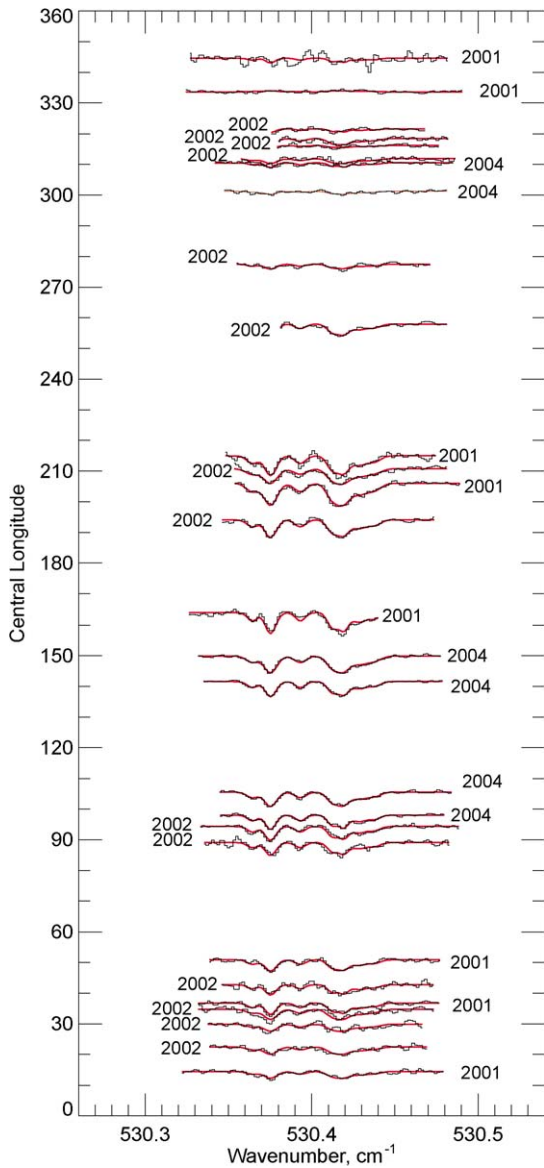


Fig. 12. Model fits to the strongest  $530.42\text{-cm}^{-1}$  band for all our Io spectra, arranged by longitude and identified by year. The smooth red lines are the models and the stair-step black lines are the data.

Lellouch, 1996), and as our modeling shows (Figs. 3, 9–11) emission lines are also possible in the mid-IR for some atmospheric conditions. The fact that emission lines are not observed on Io therefore immediately rules out models (other than the end-member volcanic-atmosphere-only models shown in Fig. 10) having simultaneously subsolar or equatorial column densities greater than about  $10^{17}\text{ cm}^{-2}$  and kinetic temperatures greater than about 250 K, a region where emission is seen in all our atmospheric models (Figs. 9 and 11).

All  $\text{SO}_2$  lines are unresolved in our data. In the mm region, Io's  $\text{SO}_2$  emission lines have a FWHM of about  $0.8\text{ km s}^{-1}$  (Lellouch et al., 1992), and may be broadened due to saturation, so the mid-IR lines, which have an optical depth typically 5 times lower, should be intrinsically

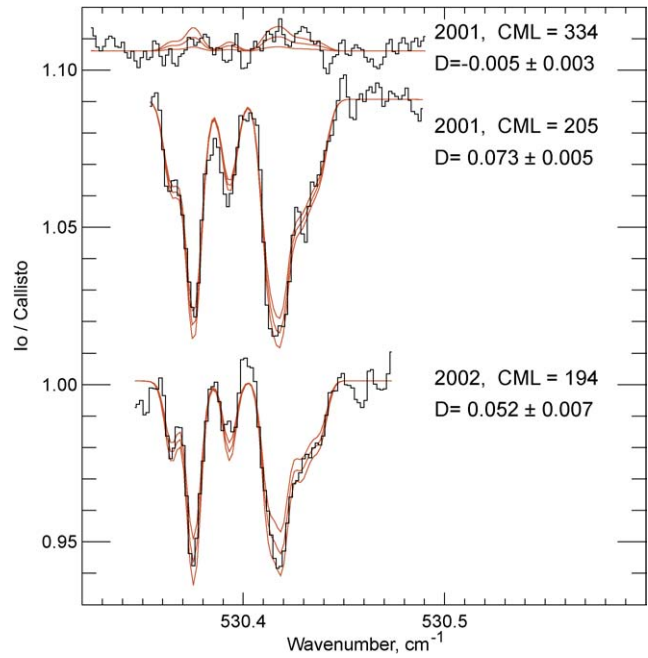


Fig. 13. Example model fits to three of the most interesting TEXES spectra. These are the 2001 and 2002 spectra of the anti-Jupiter side (central meridian longitude (CML) 194, 205) that show the clearest evidence for temporal variations (2001 being deeper), and the 2001 spectrum of the Jupiter-facing side (longitude 334) which shows tentative evidence for emission. The middle heavy smooth red line shows the best-fit model, and the flanking smooth red lines show estimated two-sigma band depth uncertainties.

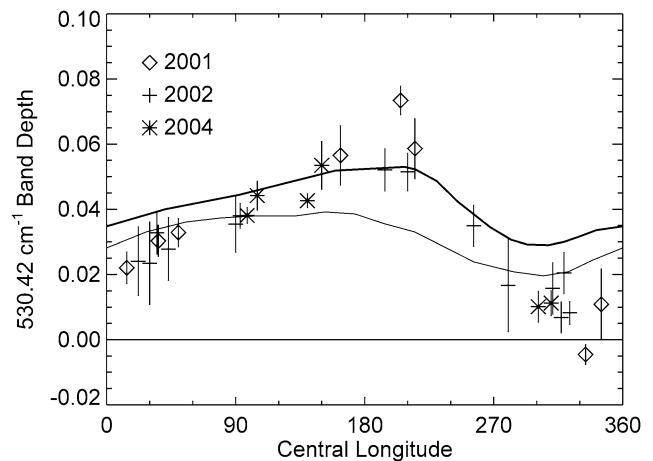


Fig. 14. Variation with longitude in the depth of the strongest  $\text{SO}_2$  band, as derived from our spectrum fits. Also shown are the longitudinal variations in the fractional coverage of NUV-bright  $\text{SO}_2$  frost as inferred from Voyager images by McEwen et al. (1988) (thin line, multiplied by 0.1) and Io's disk integrated  $3500/5500\text{ \AA}$  brightness ratio, another proxy for the coverage of bright  $\text{SO}_2$  frost, from Johnson and Pilcher (1977) (thick line, arbitrarily scaled).

narrower (unless the infrared line width reflects velocity dispersion in volcanic plumes, in which case it would be the same in the mid-IR and in the mm range). It is therefore no surprise that the lines are unresolved at the TEXES spectral resolution of  $5\text{ km s}^{-1}$ .

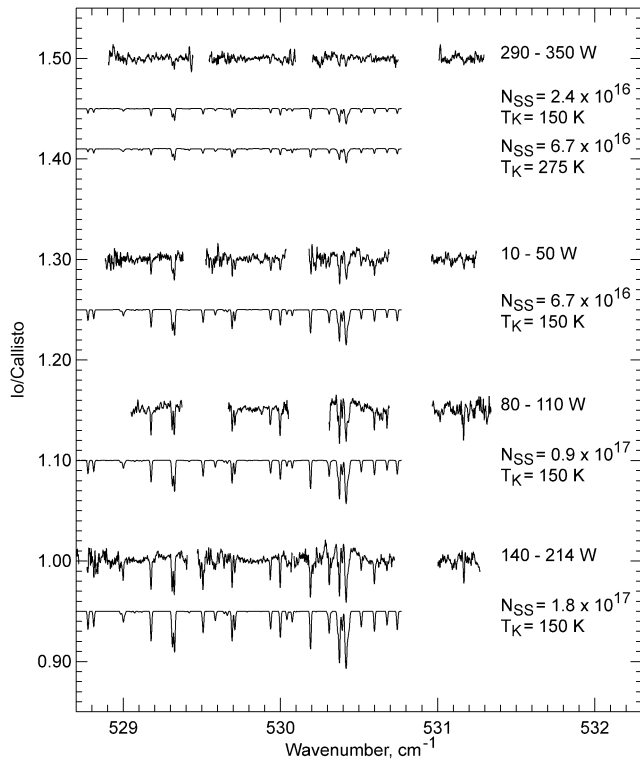


Fig. 15. Spectra averaged by longitude, combining data from all years, compared to disk-integrated models with similar line strengths. S/N varies with wavenumber because different numbers of spectra contribute to the average at each wavenumber, due to shifts in grating position (Fig. 1). Undulations in the continuum level are an artifact of the data reduction. The model spectra, based on the modified latitude model, are not formal fits to the data, but show very similar band strengths to the adjacent spectra. For the 290°–350° W spectrum, which shows the weakest lines, two quite different models are shown that both match the spectrum shape, illustrating the ambiguity in interpreting some of the spectra.

## 5.2. Longitudinal variations

Figs. 12, 14, and 15 show that the SO<sub>2</sub> line strength varies systematically and dramatically with Io's orbital longitude. The 530.42-cm<sup>-1</sup> band has a peak depth of 0.06–0.07 (at TEXES resolution) on the anti-Jupiter hemisphere near longitude 180° W, while spectral features are undetectable near longitude 300° W. As Figs. 11 and 15 show, shallow absorption lines can be a sign of either large or small gas abundance, so interpretation of this longitudinal asymmetry is ambiguous. However, we prefer the interpretation that the weak bands on the Jupiter-facing hemisphere are due to low abundance for the following reasons:

1. Fig. 11 shows that the range of density and  $T_K$  conditions in which high density or high  $T_K$  produces weak absorption lines, but does not produce emission lines, is relatively limited. For line depth to drop from 7% on the anti-Jupiter hemisphere to 1% on the Jupiter-facing hemisphere, as observed, due to an increase in density or  $T_K$  requires a rather precise tuning of atmospheric parameters—small changes in density or  $T_K$  would pro-

duce emission lines. If the weak lines are instead due to low densities, a much wider range of parameter space is available. This argument is weakened by the possible detection of emission lines in one of our spectra, at longitude 334° W in 2001 (Fig. 13), but this detection is very marginal.

2. The interpretation of high atmospheric densities on the anti-Jupiter hemisphere and lower densities on the Jupiter-facing hemisphere is consistent with HST UV disk-resolved observations, as discussed in Jessup et al. (2004). Using 2000–3000 Å spectroscopy, Jessup et al. inferred column densities of  $1.3 \times 10^{17}$  cm<sup>-2</sup> in a non-volcanic region near the subsolar point at longitude 162° W, in late 2001. In contrast, McGrath et al. (2000) used similar techniques to infer densities of  $1.5 \times 10^{16}$  cm<sup>-2</sup> near the subsolar point at longitude 300° W in mid-1996. This observation may have included a volcanic plume at Ra Patera, so density in the absence of a plume might have been even lower. While the difference between these two observations could be due to temporal rather than longitudinal variations, the lack of evidence for large temporal changes in our IR data (see below) suggests that a long-term longitudinal density asymmetry is a more likely explanation. A similar asymmetry is inferred from 1999 mm-wave data (McGrath et al., 2004). There is also evidence for greater atmospheric density and extent on the anti-Jupiter hemisphere in Ly- $\alpha$  images, which show a larger and darker region of low-latitude absorption on this hemisphere (Jessup et al., 2004; Feaga et al., 2004). As models (Strobel et al., 1994; Wong and Smyth, 2000) predict that thinner atmospheres should have a higher  $T_K$ , the marginal emission detection at longitude 334° W, mentioned above, could possibly imply an atmosphere at this longitude that is both thinner and warmer than elsewhere on Io.

While the UV spectroscopy produces less ambiguous atmospheric density information, the IR data provide better longitude and temporal coverage. Taken together, they suggest that Io's atmosphere has a large long-lived density enhancement on the side facing away from Jupiter.

It is interesting to compare the longitudinal variation in SO<sub>2</sub> line strength with the global distribution of SO<sub>2</sub> frost. While NIMS spectra show that SO<sub>2</sub> frost in some form appears to be ubiquitous on Io (Douté et al., 2001), the distribution of optically thick frost deposits that are bright in the near UV near 3500 Å (where SO<sub>2</sub> frost is bright but sulfur is dark) is very patchy and uneven. Fig. 14 also shows the fractional coverage of NUV-bright SO<sub>2</sub> frost inferred from Voyager images by McEwen et al. (1988), which like the SO<sub>2</sub> gas line strength peaks on the anti-Jupiter side and has a deep minimum near longitude 300° W. The disk integrated 3500/5500 Å brightness ratio derived from ground-based observations (Johnson and Pilcher, 1977), also a proxy for the distribution of NUV-bright frost, matches the SO<sub>2</sub> line

strength distribution even more closely. These correlations, though not perfect, suggest a connection between the spatial distribution of SO<sub>2</sub> frost and gas.

### 5.3. Atmospheric temperature and absolute abundance constraints

Fig. 11 shows that conversion of mid-IR band strengths into column abundances requires some knowledge of the atmospheric kinetic temperature  $T_K$ . The best available independent constraint comes from HST UV spectroscopy, where  $T_K$  is constrained by fitting the observed shape of the SO<sub>2</sub> absorption bands. Jessup et al. (2004) found a best-fit  $T_K$  of 200–250 K between latitudes 20° N and 20° S, and McGrath et al. (2000) determined  $T_K = 150$  K near the subsolar point at Ra Patera, though temperature at the volcanic plume Pele was higher, about 280 K. As with the mid-IR data, the UV temperature determination refers to the lowest 1–2 scale heights ( $\leq 30$  km) which dominate the vertically-integrated spectrum. The observations are consistent with the models of Strobel et al. (1994), who predicted atmospheric temperatures below 200 K in this altitude range in the absence of Joule or plasma heating. Strobel et al. (1994) and Wong and Smyth (2000) predict lower-atmosphere temperatures above 200 K when plasma or Joule heating are included. For example, Wong and Smyth obtained temperatures at 10 km altitude of about 250 K for a subsolar column density of  $5 \times 10^{17}$  cm<sup>-2</sup> and about 500 K for a column density of  $6 \times 10^{16}$  cm<sup>-2</sup>.

Fig. 11 implies that the simple incidence-dependent atmospheric model, where the atmosphere is supported by sublimation of frost with zero thermal inertia, and thus has a column density that depends only on distance from the subsolar point, is difficult to reconcile with observational constraints. Because this model concentrates the atmosphere near the subsolar point, disk-integrated abundance is smaller for a given subsolar abundance than for the latitude-dependent models. The observed peak disk-integrated 530.42-cm<sup>-1</sup> band depth of 7.3% requires subsolar column densities of at least  $5.2 \times 10^{17}$  cm<sup>-2</sup>, much higher than the HST anti-Jupiter hemisphere value of  $1.3 \times 10^{17}$  cm<sup>-2</sup> (Jessup et al., 2004), even for a low atmospheric kinetic temperature  $T_K$  of 100 K. Higher atmospheric temperatures require even larger column abundances. As previously noted, the incidence-dependent model is also not favored by the HST Ly- $\alpha$  images of Io (Feldman et al., 2000; Strobel and Wolven, 2001; Feaga et al., 2004), which appear to show dawn-to-dusk low-latitude absorption by the atmosphere.

The uniform-atmosphere model gives the strongest absorptions but is highly unrealistic, so we will concentrate on the latitude-dependent models. These are consistent with our knowledge of the atmospheric distribution, and predict band strengths more consistent with those observed. The modified-latitude model is our preferred model as it is the most consistent with the Jessup et al. (2004) data, but the

simple latitude model gives bands that are only slightly weaker (Fig. 11).

However, Fig. 16 shows that for our nominal modified-latitude model, the maximum observed 530.42-cm<sup>-1</sup> band strength of 0.073, seen on the anti-Jupiter hemisphere, can only be achieved for  $T_K \leq \sim 140$  K. Fig. 16 also shows that the thermal emission from Io's largest hot spot, Loki, will boost band depths slightly, so that the observed band depths can be generated with  $T_K = 150$  K. However Loki's longitude (310° W), means that it does not contribute to the band strength on the anti-Jupiter hemisphere. The mid-IR observations with the strongest bands, from November 2001, are almost simultaneous with the Jessup et al. (2004) anti-jovian UV HST observations, taken in November–December 2001, that give  $T_K = 200$ –250 K. Time variability in atmospheric temperature is thus probably not the explanation for the discrepancy between the UV and IR atmospheric temperatures. More likely, the inconsistent temperatures result from the limitations of both the mid-IR and UV spectroscopic models, for instance the assumption of a vertically-isothermal atmosphere in both cases, or the assumption in our model that the atmosphere over the low-temperature hot spots, which generate half of the 19- $\mu$ m flux, is representative of the atmosphere away from the hot spots.

Models where the atmosphere exists only over the 8% of the surface occupied by hot spots (Fig. 10) predict column densities over the hot spots that are similar to those predicted for the entire surface in our standard model, and thus regionally-averaged column densities that are an order of magnitude lower than our standard model. These models are not realistic, because an atmosphere covering only 8% of the surface could not produce the strong equatorial absorption seen in the Lyman- $\alpha$  images, and would be difficult to reconcile with the UV spectroscopic observations. However the models do provide a lower limit to the regionally-averaged

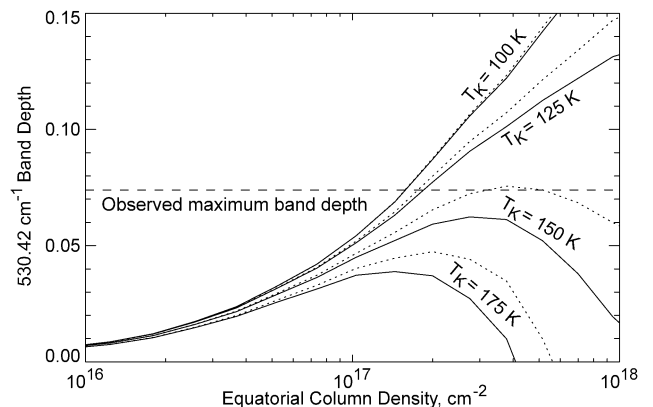


Fig. 16. Relationship between model band depth and equatorial column density, as a function of assumed atmospheric kinetic temperature  $T_K$ . The solid lines are for our nominal (modified latitude) model, and dashed lines are for the Loki hemisphere model (Fig. 9, lower left) which shows the strongest bands of any of our models. Model  $T_K$  must be lower than about 140 K (150 K for the Loki hemisphere model) to match the maximum observed band strengths.

gas abundances that can be inferred from the 19- $\mu\text{m}$  observations. Note that even in the volcanic-only models, the observed peak 530.42- $\text{cm}^{-1}$  band strength of 7% requires quite low atmospheric kinetic temperatures: 175 K if all hot spots have the same gas abundance, and about 160 K if the hot spot atmosphere are concentrated at low latitudes, unless the equatorial column density exceeds  $10^{18} \text{ cm}^{-2}$ .

Assuming an atmospheric kinetic temperature of 125 K, close to the maximum consistent with observed band depths, and also assuming our preferred modified-latitude model, Fig. 17 shows the equatorial column density as a function of longitude derived from the band depths shown in Fig. 14. Note that for simplicity the relationship between band strength and column density is derived from the modified-latitude model calculated at the standard longitude ( $180^\circ \text{ W}$ ) and heliocentric distance (5.30 AU) for all data: Fig. 9 shows that errors resulting from this approximation are probably small compared to other uncertainties. With these assumptions, equatorial column density then varies from  $\sim 1.5 \times 10^{17} \text{ cm}^{-2}$  on the anti-Jupiter hemisphere to  $\sim 1.5 \times 10^{16} \text{ cm}^{-2}$  at longitude 300. The longitudinal variation is remarkably consistent, considering the model assumptions and very different techniques used, with abundances derived from the disk-resolved HST UV spectroscopic data also plotted on Fig. 17.

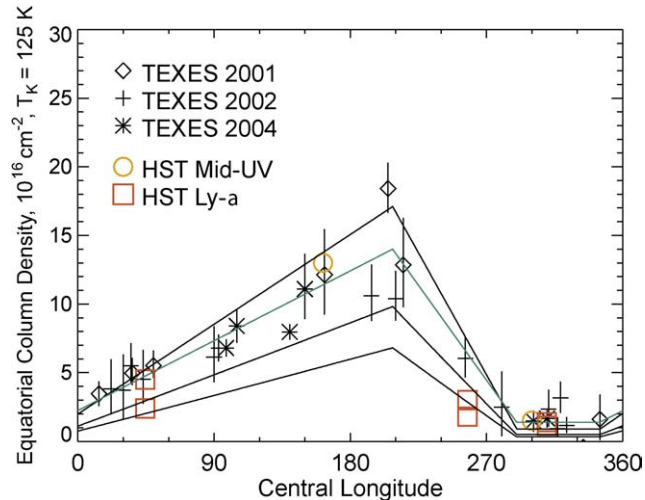


Fig. 17. Distribution of equatorial column density with longitude for our three years of data, determined from observed band strength (Fig. 14) assuming  $T_K = 125 \text{ K}$ . Also shown are the two disk-resolved HST UV spectroscopic observations of the column density near the subsolar point (McGrath et al., 2000; Jessup et al., 2004), which agree remarkably well with the densities inferred from the mid-IR data, and subsolar column densities estimated from Lyman- $\alpha$  images (Feldman et al., 2000). The uppermost black line shows a piecewise-linear approximate fit to the 2001 longitudinal variations. The two lower black lines show this curve adjusted to the expected column density in 2002 and 2004, on the assumption that the top curve describes the 2001 data, and the atmosphere is supported by  $\text{SO}_2$  frost in equilibrium with sunlight, which cools as Io recedes from the Sun. Though anti-jovian column densities did drop by about the expected amount between 2001 and 2002, the expected column density drop is not seen at other longitudes, or between 2002 and 2004. The green line shows an approximate fit to the data from all three years.

#### 5.4. Comparison with millimeter and Lyman- $\alpha$ data

Comparing our results with those obtained from the millimeter data (Lellouch et al., 1992, 2003; Lellouch, 1996; McGrath et al., 2004) is not straightforward given the different data characteristics. First, the mm data primarily sample the leading and trailing sides, and do not easily provide information on the Jupiter-facing and anti-Jupiter hemispheres because of contamination by Jupiter radiation. Early observations (Lellouch et al., 1992), analyzed assuming hydrostatic equilibrium, indicated a dense  $1.5\text{--}8.0 \times 10^{17} \text{ cm}^{-2}$ , very localized (covering 2.5–4% of the disk), and hot (500–600 K) atmosphere on Io's trailing side. Further observations in 1993 and 1994 indicated a somewhat cooler (250–400 K) and more extended (12–16%) atmosphere on the leading side (Lellouch, 1996). Hemispherically-averaged columns are of order  $1\text{--}2 \times 10^{16} \text{ cm}^{-2}$ . The need for such high temperatures and very localized atmospheres can be relaxed by assuming that the line widths reflect velocity dispersion in plumes, but the average columns remain roughly the same. In our preferred modified-latitude model for interpreting the 19- $\mu\text{m}$  data, the hemispherically-averaged column density is  $6 \times 10^{16} \text{ cm}^{-2}$  at CML = 90 (leading side) and  $5 \times 10^{16} \text{ cm}^{-2}$  at CML = 270 (trailing side), a few times higher than the above mm-derived number. This discrepancy could be simply due to temporal variability, or might for instance imply that the atmosphere is concentrated over hot spots, contrary to our assumption in modeling the mid-IR data that the atmospheric distribution is smooth. The discrepancy demonstrates the limits of our current ability to interpret the disparate UV, IR, and mm data.

High S/N millimeter observations acquired in 1999 have permitted searches for variations of the strong  $\text{SO}_2$  mm lines over a significant fraction of Io's orbit with an orbital longitude resolution of  $10^\circ\text{--}20^\circ$ . These indicate an increase of the line areas as central longitude increases from  $45^\circ$  to  $135^\circ \text{ W}$ , and a decrease in line areas as longitude increases from  $240^\circ$  to  $340^\circ \text{ W}$  (see Fig 19.6 of McGrath et al., 2004). Although the line area is not a direct indicator of the  $\text{SO}_2$  abundance, this behavior is generally consistent with the longitudinal variation indicated by our new infrared data, and in particular our finding of a denser atmosphere on Io's anti-Jupiter hemisphere. In contrast, the atmospheric temperature remains extremely uncertain, as recent mm data from 2002 indicate cooler temperatures than implied before, even if interpreted with a static atmosphere model. The high-quality 1999 mm observations implied  $T_K = 400 \pm 100 \text{ K}$  on the trailing side, while the 2002 observations implied a leading/trailing mean temperature of only  $180 \pm 60 \text{ K}$  (Lellouch et al., 2003; McGrath et al., 2004). Only the latter figure is consistent with our requirement of a  $T_K < 140 \text{ K}$ . Possibly the atmosphere has been cooler in the 2001–2004 period of the infrared observations, and the latest mm data, than in previous years. We also note that the millimeter data provide a lower limit of the bulk gas temperature, based on the emission contrasts at Io of the strongest lines (20–40 K, de-

pending on the year). Assuming a mm continuum brightness temperature of 88 K (Altenhoff et al., 1988), this gives a hard lower limit of 108–128 K. Although this does not seem to contradict  $T_K < 140$  K, this lower limit actually holds for a globally uniform atmosphere, a quite unlikely situation as discussed before. For an optically thick atmosphere covering a  $\pm 30^\circ$  latitude band, the temperature lower limit becomes 121–154 K. Checking the consistency of the mid-IR data with the mm data will require attempting fits of the latter with the global atmospheric models developed in this paper.

Another source of SO<sub>2</sub> column abundance information is the HST Lyman- $\alpha$  imaging, where subsolar gas abundance can be estimated from the brightness of the center of Io's disk. Abundance estimates depend on assumptions about Io's equatorial albedo at 1216 Å, and the brightness of the interplanetary Ly- $\alpha$  background behind Io. Reasonable albedo assumptions yield abundances in the range  $1.4\text{--}4.5 \times 10^{16}$  cm<sup>-2</sup> for zero interplanetary background, or  $1.1\text{--}2.4 \times 10^{16}$  cm<sup>-2</sup> for a 300 Rayleigh background, for images taken at central longitudes between 243° and 53° W in 1997 and 1998 (Feldman et al., 2000). These abundances are comparable to or somewhat smaller than those derived from the mid-IR data at similar longitudes (Fig. 17). Jessup et al. (2004) noted that HST Lyman- $\alpha$  images taken over a range of longitudes and years qualitatively confirmed the existence and stability of the longitudinal SO<sub>2</sub> gas asymmetry that was inferred in that paper from 2000–2300 Å HST spectra, and which is revealed in more detail by the 19- $\mu$ m spectra reported here. More comprehensive and quantitative recent analysis of the full set of available HST Lyman- $\alpha$  images (Feaga et al., 2004) adds more detail to the picture, and confirms the presence of a strong maximum in SO<sub>2</sub> abundance on the anti-Jupiter hemisphere, correlated with the SO<sub>2</sub> frost distribution and stable over several years. However, subsolar column densities on the anti-Jupiter hemisphere derived by Feaga et al. from the Lyman- $\alpha$  images, derived on the assumption of uniform surface albedo, are still about a factor of two lower than those derived from the 19  $\mu$ m and 2000–2300 Å spectroscopy. Possibly the Lyman- $\alpha$  derived abundances are too low because of latitudinal variations in surface albedo or the assumption that the atmosphere is homogeneous at sub-HST resolution (McGrath et al., 2004), or our 19- $\mu$ m-derived abundances are too high because of concentration of the atmosphere over hot spots, as previously discussed.

### 5.5. Time variations?

The variation of 530.42-cm<sup>-1</sup> band strength with longitude (Fig. 14) is remarkably stable over the two-year time span of our observations. Several previous data sets from the 1990s (Lellouch, 1996; Jessup et al., 2002; McGrath et al., 2004) have shown up to two-fold temporal variability in atmospheric column density, though quantitative comparisons are often difficult due to uncertainties in interpretation. Ignoring heliocentric distance effects discussed

below, the stability seen in the recent IR data may be easiest to understand if the atmosphere seen at 19  $\mu$ m is primarily supported by frost sublimation, because of the long-term stability of albedo patterns on Io (Geissler et al., 1999b). Because Prometheus-type plumes have typical lifetimes of several years (McEwen and Soderblom, 1983; Keszhelyi et al., 2001), the observed stability may also be consistent with volcanic support, though there is considerable variability in thermal infrared emission even from long-lived plume sources like Prometheus (Davies, 2003), with likely corresponding variability in gas output. Unfortunately we have only sporadic data on the longitudinal distribution of volcanic or plume activity during the period of these observations. The last successful close-up Galileo observations were in October 2001, and while a global map of Io's 3.5- $\mu$ m thermal emission was obtained by Keck in December 2001, shortly after our first 19- $\mu$ m observations (LeMignant et al., 2002), this is of limited use because there does not appear to be good correlation between thermal IR emission and plume activity. For instance, Loki is frequently the brightest volcanic source of 3.5- $\mu$ m radiation on Io but has not been a significant plume source during the Galileo era.

Only the anti-jovian hemisphere of Io shows evidence for time variability of band strength, from 7.3% near longitude 200° W in 2001 to 5.2% in 2002 (Fig. 13), corresponding to a column density drop from  $\sim 1.8 \times 10^{17}$  to  $\sim 1.4 \times 10^{17}$  cm<sup>-2</sup> given the assumptions in Fig. 17. One possible explanation for the drop in band strength is the increase in Io's heliocentric distance from 2001 to 2002: if the atmosphere was supported by vapor pressure equilibrium with sunlight, the density of the atmosphere should decrease as Io recedes from the Sun (Table 1) and the frost temperature decreases. Fig. 17 shows the expected change in column density for a sublimation-supported atmosphere between 2001, 2002, and 2004. While the 2001–2002 change on the anti-jovian hemisphere is consistent with sublimation support, there is no evidence for the expected further change from 2002–2004 (though limited longitude coverage in 2004 makes comparison difficult), and no evidence for any change on the leading hemisphere, where longitude and temporal coverage is good.

### 5.6. Sublimation vs volcanic support of the SO<sub>2</sub> atmosphere

We are still faced with conflicting evidence regarding the dominant process supporting Io's atmosphere. Although active volcanism is presumably the ultimate source of all the SO<sub>2</sub>, the question of whether the immediate source of the atmospheric SO<sub>2</sub> is dominated by volcanic vents or subliming frost is physically significant, especially in terms of vertical structure, lifetime, response to diurnal or eclipse variations in insolation, and radiative and photochemical properties.

The apparent lack of diurnal variation in atmospheric density inferred from the Lyman- $\alpha$  images is a natural con-

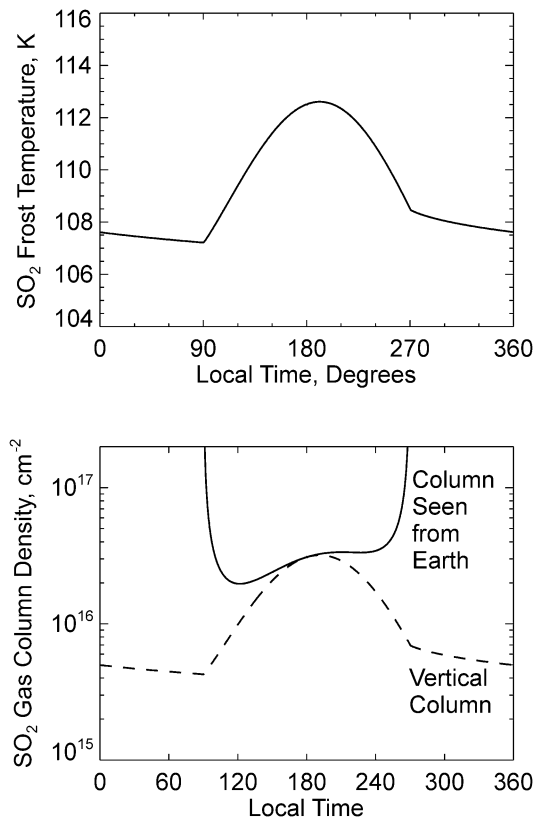


Fig. 18. Diurnal variations in surface temperature for high thermal inertia  $\text{SO}_2$  frost, and corresponding equilibrium  $\text{SO}_2$  gas column density, showing how significant gas column density can be maintained from dawn to dusk by sublimation of high thermal inertia frost when the effects of increasing atmospheric path length near the dawn and dusk limb as seen from Earth are included, calculating airmass using a simple  $1/\cos(i)$  rule which is adequate for this purpose. The frost model has a substrate with thermal inertia  $2 \times 10^{16} \text{ erg cm}^{-2} \text{ s}^{-1/2} \text{ K}^{-1}$ , overlain by a 1.5 cm layer with thermal inertia  $1.3 \times 10^5 \text{ erg cm}^{-2} \text{ s}^{-1/2} \text{ K}^{-1}$ . Albedo is 0.5, and emissivity is 1.0. Local time is defined to be zero at midnight, so a local time of  $180^\circ$  corresponds to local noon.

sequence of the volcanic support model (Strobel and Wolven, 2001). However, sublimation support by high thermal inertia frost could possibly also produce dawn-to-dusk atmospheric absorption, particularly when the effects of increasing airmass near the limb, as seen from Earth, are included. For instance, Fig. 18 shows a model in which the slant equatorial column density of a sublimation-supported  $\text{SO}_2$  atmosphere, as seen from Earth, is never less than 60% of the subsolar value. The model frost surface has two-layer vertical structure, which reduces the strong morning/afternoon temperature asymmetry seen in single-layer models. The substrate thermal inertia is comparable to that of solid water ice (Spencer et al., 1997), while the upper layer thermal inertia is intermediate between solid ice and the  $7 \times 10^4 \text{ erg cm}^{-2} \text{ s}^{-1/2} \text{ K}^{-1}$  thermal inertia of Io's average surface (Rathbun et al., 2004). Effective thermal inertia could be high due to grain sintering (Sandford and Allamandola, 1993; Geissler et al., 2001b) and/or solid-state greenhouse effects (Trafton et al., 1998).

The lack of correlation between inferred atmospheric density and heliocentric distance, except perhaps between 2001 and 2002 on the anti-Jupiter hemisphere (Fig. 17), is difficult to explain if the atmosphere is supported by frost sublimation, and is thus an argument for volcanic support. However, because the mid-IR observations are biased towards the atmosphere over low-temperature hot spots (Fig. 6), it is possible that there are volcanically supported atmospheres over these hot spots but a more widespread sublimation-supported atmosphere away from the hot spots, to which the mid-IR data are less sensitive. It's also possible that high frost thermal inertia can reduce the amplitude of frost seasonal temperature variations, as may happen on Triton (Spencer and Moore, 1992), but further modeling is needed to investigate this possibility.

2000–3000 Å disk-resolved spectroscopy of the atmosphere provides arguments for sublimation support. At low latitudes near  $160^\circ \text{ W}$  there is quantitative agreement between latitudinal variations in column density and simple sublimation support models, apart from a relatively modest enhancement at the Prometheus plume (Jessup et al., 2004 and Fig. 7) and enhancements at mid-latitudes that may be due to hydrodynamic spreading of the atmosphere away from the subsolar point (Wong and Johnson, 1996; Wong and Smyth, 2000; Austin and Goldstein, 2000). The smooth variation in abundance with latitude seen by Jessup et al. is difficult to reconcile with volcanic support because volcanic atmospheres are expected to drop off rapidly, on 100-km length scales, away from volcanic sources (Zhang et al., 2003).

There is evidence for sublimation support on the opposite, Jupiter-facing side of Io, provided by the observation that neutral atomic emissions from Io decrease significantly in Jupiter eclipse (Clarke et al., 1994; Retherford, 2002; Geissler et al., 2004). Saur and Strobel (2004) infer from the eclipse-related changes that about 90% of the daytime atmosphere is sublimation supported, and while this number is model-dependent, it is difficult to reconcile a purely volcanic atmosphere with the eclipse-induced changes in the atomic emissions.

The correlation between the longitudinal distribution of optically thick, NUV-bright  $\text{SO}_2$  frost and  $\text{SO}_2$  gas does not unambiguously point to volcanic or sublimation control of the atmosphere. This correlation could be due to support of the atmosphere by sublimation of the NUV-bright frost, or the development of NUV-bright frost patches by atmospheric condensation at longitudes where a volcanically-supported atmosphere is densest.

The longitudes with lower atmospheric density and less  $\text{SO}_2$  frost are also the longitudes with the fewest Prometheus-type plumes (McEwen and Soderblom, 1983), but this could be because Prometheus-type plumes appear to form from interaction of lava flows with surface frost (Milazzo et al., 2001), and there is simply less frost for lava flows to interact with in these regions.

## 6. Summary

Mid-infrared spectroscopy of the  $\nu_2$  SO<sub>2</sub> band provides a new window on Io's atmosphere. While the spectra suffer some ambiguity in interpretation (due to the strong dependence of line strength on surface and atmospheric temperatures), they provide better longitudinal and temporal monitoring than most previous techniques. Dramatic variations in line strength with longitude are seen that are stable over at least a 2-year period, with the strongest bands being found on the anti-Jupiter hemisphere. The most plausible interpretation of band strength in terms of SO<sub>2</sub> column density suggests that the atmosphere is about ten times denser on the anti-Jupiter side, than near longitude 300° W, as also suggested by HST observations. The atmospheric distribution follows the longitudinal distribution of bright, optically thick, SO<sub>2</sub> frost.

Combining the HST constraints on latitudinal distribution (using our preferred “modified latitude” model which best fits the most recent HST observations (Jessup et al., 2004)), and the combined HST/IR constraints on longitudinal distribution, we can produce a first-order global map of daytime atmospheric column density (Fig. 19). This model fits all the HST disk-resolved spectroscopic observations of atmospheric density to within a factor of two or better. While this map is undoubtedly crude (for instance, the sharply-bounded plateau in abundance at mid-latitudes assumed by the modified-latitude model is undoubtedly unrealistic), it provides a model against which additional data sets can be compared in order to improve the model further. Fig. 19 suggests that while the gradient in SO<sub>2</sub> abundance from  $1.5 \times 10^{16} \text{ cm}^{-2}$  at Ra (7° S, 318° W) to  $3.2 \times 10^{16} \text{ cm}^{-2}$  at Pele (18° S, 257° W) seen by McGrath et al. (2000) could be due to outgassing at Pele, the gradient could also be part of a regional increase in atmospheric density with decreasing longitude on this side of Io, unrelated to activity at Pele it-

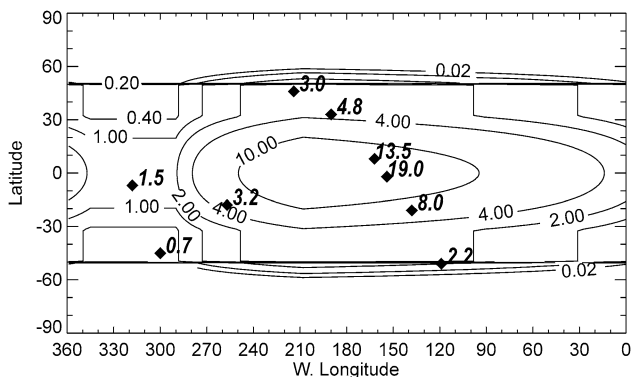


Fig. 19. A crude empirical global model for the distribution of Io's day-side atmosphere, in units of  $10^{16} \text{ cm}^{-2}$  vertical column abundance of SO<sub>2</sub>, derived by combining the longitudinal variation in equatorial abundance inferred from the 19- $\mu\text{m}$  data (green line, Fig. 17) and the modified-latitude model of the latitudinal variation (Fig. 17). Solid diamonds show observations of the column abundance derived from 2000–3000 Å disk-resolved HST spectroscopy, from McGrath et al. (2000) (longitudes 260°–320° W) and Jessup et al. (2004) (longitudes 120°–220° W).

self which may or may not have been active during the 1996 observations.

The observed maximum mid-IR line strengths seem to require atmospheric kinetic temperatures colder than 150 K, which is lower than theoretical expectations and at least some HST and millimeter spectroscopic determinations of kinetic temperature.

## Acknowledgments

We thank TEXES PI John Lacy, and the IRTF telescope operators, Bill Golisch, Dave Griep, and Paul Sears for their assistance at the telescope, and Andy Ingersoll, Paul Geissler, and Gilda Ballester for helpful reviews. John Spencer and Kandis Lea Jessup were funded by NASA Grants NAG5-10497, NAG5-13350, and NAG5-9004. The fabrication of TEXES was supported primarily by the National Science Foundation, with additional support from the National Aeronautics and Space Administration through the Universities Space Research Association. Observations with TEXES were supported by the Texas Advanced Research Program. Thomas Greathouse was supported by the Lunar and Planetary Institute, which is operated by the Universities Space Research Association under NASA CAN-NCC5-679. This paper represents LPI Contribution 1233.

## Appendix A. Spectral line parameters of sulfur dioxide in the 19- $\mu\text{m}$ spectral region

In the 19- $\mu\text{m}$  spectral region the main absorbing SO<sub>2</sub> band is the cold  $\nu_2$  band but, given the lower value of the vibrational energy of the (010) state ( $\sim 517.9 \text{ cm}^{-1}$ ) the associated hot bands  $2\nu_2-\nu_2$  and  $3\nu_2-2\nu_2$  exhibit non negligible absorptions and are also easily observable at room temperatures or below. The available HITRAN data dates back to one of the first releases of the database (Rothman et al., 1987) and concerns only the  $\nu_2$  band. More recent high resolution studies dealing with the 19- $\mu\text{m}$  SO<sub>2</sub> absorptions have been performed leading to much more precise line positions (Coudert et al., 1987; Flaud et al., 1993). A series of low resolution band intensity measurements have been performed (see Pugh and Narahari Rao (1976) and Smith et al. (1992) for a compilation of results) as well as a study of individual line intensities (Sumpf, 1999).

### A.1. Line position

Sumpf (1999) noted that “the calculation of the SO<sub>2</sub> spectrum based on the HITRAN database shows a remarkably different pattern without any similarity with the observed spectrum” preventing any reliable assignment. In the 19- $\mu\text{m}$  region we found the HITRAN line positions to differ from those observed on Io by about  $0.12 \text{ cm}^{-1}$ . However, a good agreement is observed when using recent data (Flaud

Table 2  
Summary of the band intensity calculations for  $^{32}\text{SO}_2$

Band assignment	Total band intensity <sup>a</sup>	Maximum line intensity <sup>a</sup>	Number of lines
$\nu_2$	$0.392 \times 10^{-17}$	$0.721 \times 10^{-20}$	5914
$2\nu_2 - \nu_2$	$0.610 \times 10^{-18}$	$0.116 \times 10^{-20}$	3727
$3\nu_2 - 2\nu_2$	$0.591 \times 10^{-19}$	$0.014 \times 10^{-20}$	1532

<sup>a</sup> The intensities are given at 296 K in  $\text{cm}^{-1}/(\text{molecule cm}^{-2})$ .

et al., 1993). The authors calculated the new line positions using a Hamiltonian model which accounts for the various ro-vibrational resonances which affect the energy levels. As a consequence we can estimate the accuracy on the new line positions to be about  $10^{-3} \text{ cm}^{-1}$  or better.

### A.2. Line intensities

The average of the measured integrated band intensities (Pugh and Narahari Rao, 1976; Smith et al., 1992) corresponds to an intensity of  $0.392 \pm 0.06010^{-17} \text{ cm}^{-1}/(\text{molecule cm}^{-2})$  for the  $\nu_2$  band of  $^{32}\text{S}^{16}\text{O}_2$  and this value is not very different from the value used in the HITRAN database. However it should be noted that the average value of the ratio of the individual line intensities measured by Sumpf (1999), ( $S_{\text{meas}}/S_{\text{HITRAN}}$ ) is  $0.61 \pm 0.10$ , showing a clear inconsistency. We have no explanation for such a discrepancy but, given the rather large number of low resolution measurements, we decided to scale our calculation to the band intensity they provided.

The intensity  $k_{\tilde{\nu}}$  of an individual line can be written as:

$$k_{\tilde{\nu}} = 8\pi^3 \tilde{\nu} / (4\pi\epsilon_0 3hcZ(T)) g (1 - \exp(-hc\tilde{\nu}/kT)) \times \exp(-hcE_A/kT) R_A^B$$

(Flaud et al., 1981; Camy-Peyret and Flaud, 1985), where A and B are, respectively, the lower and upper levels of the transition,  $g$  is the nuclear statistical weight,  $\tilde{\nu} = (E_B - E_A)/hc$  is the wavenumber of the transition and  $Z(T)$  is the total partition function.

Finally,  $R_B^A$  is the square of the matrix element of the transformed dipole moment operator  $\mu'_Z$  (Flaud et al., 1981; Camy-Peyret and Flaud, 1985):

$$R_B^A = |\langle v', J'K'_aK'_c | \mu'_Z | v'', J''K''_aK''_c \rangle|.$$

The calculation of the matrix elements of  $\mu'_Z$  is extensively described in Flaud et al. (1981) and Camy-Peyret and Flaud (1985) and it is only necessary here to stress that we used the wavefunctions derived from the energy level calculations to calculate the matrix elements. In this way one takes into account the effect of the resonances on the line intensities. Table 2 summarizes the results.

## References

Altenhoff, W.J., Chini, R., Hein, H., Kreysa, E., Mezger, P.G., Salter, C., Schraml, J.B., 1988. First radio astronomical estimate of the temperature of Pluto. *Astron. Astrophys.* 190, L15–L17.

- Austin, J.V., Goldstein, D.B., 2000. Rarefied gas model of Io's sublimation-drive atmosphere. *Icarus* 148, 370–383.
- Ballester, G.E., Moos, H.W., Feldman, P.D., Strobel, D.F., Summers, M.E., Bertaux, J.-L., Skinner, T.E., Festou, M.C., Lieske, J.H., 1987. Detection of neutral oxygen and sulfur emissions near Io using IUE. *Astrophys. J.* 319, L33–L38.
- Ballester, G.E., McGrath, M.A., Strobel, D.F., Zhu, X., Feldman, P.D., Moos, H.W., 1994. Detection of the  $\text{SO}_2$  atmosphere on Io with the Hubble Space Telescope. *Icarus* 111, 2–17.
- Bass, H.E., Winter, T.G., Evans, L.B., 1971. Vibrational and rotational relaxation in  $\text{SO}_2$ . *J. Chem. Phys.* 54, 644–647.
- Bouchez, A.H., Brown, M.E., Schneider, N.M., 2000. Eclipse spectroscopy of Io's atmosphere. *Icarus* 148, 316–319.
- Camy-Peyret, C., Flaud, J.-M., 1985. Vibration–rotation dipole moment operator for asymmetric rotors. In: Narahari Rao, K. (Ed.), *Molecular Spectroscopy: Modern Research*, vol. 3. Academic Press, New York.
- Clarke, J., Ajello, J., Luhmann, J., Schneider, N., Kank, I., 1994. Hubble Space Telescope UV spectral observations of Io passing into eclipse. *J. Geophys. Res.* 99, 8387–8402.
- Coudert, L., Maki, A., Olson, B., 1987. High-resolution measurements of the  $\nu_2$  and  $2\nu_2 - \nu_2$  bands of  $\text{SO}_2$ . *J. Mol. Spectrosc.* 124, 437–442.
- Davies, A.G., 2003. The pulse of the volcano: Discovery of episodic activity at Prometheus on Io. *Lunar Planet. Sci.* 34, Abstract 1455.
- dePater, I., Roe, H., Graham, J.R., Strobel, D.F., Bernath, P., 2002. Note: Detection of the forbidden  $\text{SO } a^1\Delta \rightarrow X^3\Sigma^-$  rovibronic transition on Io at 1.7  $\mu\text{m}$ . *Icarus* 156, 296–301.
- Douté, S., Schmitt, B., Lopes-Gautier, R., Carlson, R., Soderblom, L., Shirley, J., the Galileo NIMS Team, 2001. Mapping  $\text{SO}_2$  frost on Io by the modeling of NIMS hyperspectral images. *Icarus* 149, 107–132.
- Fanale, F.P., Banerdt, W.B., Elson, L.S., Johnson, T.V., Zurek, R.W., 1982. Io's surface—Its phase composition and influence on Io's atmosphere and Jupiter's magnetosphere. In: *Satellites of Jupiter*. Univ. of Arizona Press, Tucson, pp. 756–781.
- Feaga, L.M., McGrath, M.A., Feldman, P.D., Strobel, D.F., 2004. Dependence of Io's  $\text{SO}_2$  atmospheric column density on surface features. *Bull. Am. Astron. Soc.* 36, 1099.
- Feldman, P.D., Strobel, D.F., Moos, H.W., Retherford, K.D., Wolven, B.C., McGrath, M.A., Roesler, F.L., Woodward, R.C., Oliverson, R.J., Ballester, G.E., 2000. Lyman-alpha imaging of the  $\text{SO}_2$  distribution on Io. *Geophys. Res. Lett.* 27, 1787–1789.
- Flaud, J.-M., Camy-Peyret, C., Toth, R.A., 1981. *Water Vapor Line Parameters from Microwave to Medium Infrared*. Pergamon, Oxford.
- Flaud, J.-M., Perrin, A., Salah, L.M., Lafferty, W.J., Guelachvili, G., 1993. A reanalysis of the (010), (020), (100), and (001) rotational levels of  $^{32}\text{S}^{16}\text{O}_2$ . *J. Mol. Spectrosc.* 160, 272–278.
- Geissler, P.E., McEwen, A.S., Ip, W., Belton, M.J.S., Johnson, T.V., Smyth, W., Ingersoll, A.P., 1999a. Galileo imaging of atmospheric emissions from Io. *Science* 285, 870–874.
- Geissler, P.E., McEwen, A.S., Keszthelyi, L., Lopes-Gautier, R., Granahan, J., Simonelli, D.P., 1999b. Global color variations on Io. *Icarus* 140, 265–282.
- Geissler, P., Smyth, W.H., McEwen, A.S., Ip, W., Belton, M.J.S., Johnson, T.V., Ingersoll, A.P., Rages, K., Hubbard, W., Dessler, A.J., 2001a. Morphology and time variability of Io's visible aurora. *J. Geophys. Res.* 106, 26137–26146.

- Geissler, P., McEwen, A., Phillips, C., Simonelli, D., Lopes, R.M.C., Douté, S., 2001b. Galileo imaging of SO<sub>2</sub> frosts on Io. *J. Geophys. Res.* 106, 33253–33266.
- Geissler, P., McEwen, A.S., Porco, C., Strobel, D., Saur, J., Ajello, J., West, R., 2004. Cassini observations of Io's visible aurorae. *Icarus* 172, 127–140.
- Hendrix, A.R., Barth, C.A., Hord, C.W., 1999. Io's patchy SO<sub>2</sub> atmosphere as measured by the Galileo ultraviolet spectrometer. *J. Geophys. Res.* 104, 11817–11826.
- Ingersoll, A.P., 1989. Io meteorology—How atmospheric pressure is controlled locally by volcanos and surface frosts. *Icarus* 81, 298–313.
- Jessup, K.L., Ballester, G.E., Combi, M., Zhu, X., Strobel, D.F., Clarke, J.T., 2002. Io's changing atmosphere. In: *Magnetospheres of the Outer Planets Conference Proceedings*, p. 116.
- Jessup, K.L., Spencer, J.R., Ballester, G.E., Howell, R.R., Roesler, F., Vigil, M., Yelle, R., 2004. The atmospheric signature of Io's Prometheus plume and anti-jovian hemisphere: Evidence for a sublimation atmosphere. *Icarus* 169, 197–215.
- Johnson, T.V., Pilcher, C.B., 1977. Satellite spectrophotometry and surface compositions. In: Burns, J. (Ed.), *Planetary Satellites*. Univ. of Arizona Press, Tucson, pp. 232–268.
- Keszthelyi, L., 13 colleagues, 2001. Imaging of volcanic activity on Jupiter's moon Io by Galileo during the Galileo Europa Mission and the Galileo Millennium Mission. *J. Geophys. Res.* 106, 33025–33052.
- Lacy, J.H., Richter, M.J., Greathouse, T.K., Jaffe, D.T., Zhu, Q., 2001. TEXES: A sensitive high-resolution grating spectrograph for the mid-infrared. *Publ. Astron. Soc. Pacific* 114, 153–158.
- Lellouch, E., 1996. Urey Prize lecture. Io's atmosphere: Not yet understood. *Icarus* 124, 1–21.
- Lellouch, E., Belton, M.J.S., DePater, I., Paubert, G., Gulkis, S., Encenaz, T., 1992. The structure, stability, and global distribution of Io's atmosphere. *Icarus* 98, 271–295.
- Lellouch, E., Strobel, D.F., Belton, M.J.S., Summers, M.E., Paubert, G., Moreno, R., 1996. The detection of sulfur monoxide in Io's atmosphere. *Astrophys. J.* 459, L107–L110.
- Lellouch, E., Paubert, G., Moses, J.I., Schneider, N.M., Strobel, D.F., 2003. Volcanically emitted sodium chloride as a source for Io's neutral clouds and plasma torus. *Nature* 421, 45–47.
- LeMignant, D., Marchis, F., Kwok, S., Amico, P., Campbell, R., Chaffee, F., Conrad, A., Contos, A., Goodrich, R., Hill, G., Spayberry, D., Stomski, P.J., Wizinowich, P., DePater, I., 2002. Io, the movie. *Proc. SPIE* 4834, 319–328.
- López-Puertas, M., Taylor, F.W., 2001. *Non-LTE Radiative Transfer in the Atmosphere*. World Scientific Publishing, Singapore.
- López-Valverde, M.A., López-Puertas, M., 1994. A non-local thermodynamic equilibrium radiative transfer model for infrared emissions in the atmosphere of Mars. 1. Theoretical basis and nighttime populations of vibrational levels. *J. Geophys. Res.* 99, 13093–13116.
- López-Valverde, M.A., Edwards, D.P., López-Puertas, M., Roldán, C., 1998. Non-local thermodynamic equilibrium in general circulation models of the martian atmosphere. 1. Effects of the local thermodynamic equilibrium approximation on the thermal cooling and solar heating. *J. Geophys. Res.* 103, 16799–16811.
- McEwen, A.S., Soderblom, L.A., 1983. Two classes of volcanic plumes on Io. *Icarus* 55, 191–217.
- McEwen, A.S., Soderblom, L.A., Johnson, T.V., Matson, D.L., 1988. The global distribution, abundance, and stability of SO<sub>2</sub> on Io. *Icarus* 75, 450–478.
- McGrath, M.A., Belton, M.J.S., Spencer, J.R., Sartoretti, P., 2000. Spatially resolved spectroscopy of Io's Pele plume and SO<sub>2</sub> atmosphere. *Icarus* 146, 476–493.
- McGrath, M.A., Lellouch, E., Strobel, D.F., Feldman, P.D., Johnson, R.E., 2004. Satellite atmospheres. In: Bagenal, F., Dowling, T.E., McKinnon, W.B. (Eds.), *Jupiter: The Planet, Satellites, and Magnetosphere*. Cambridge Univ. Press, Cambridge.
- Milazzo, M.P., Keszthelyi, L.P., McEwen, A.S., 2001. Observations and initial modeling of lava–SO<sub>2</sub> interactions at Prometheus, Io. *J. Geophys. Res.* 106, 33121–33128.
- Moreno, M.A., Schubert, G., Kivelson, M.G., Paige, D., Baumgardner, J., 1991. Io's volcanic and sublimation atmospheres. *Icarus* 93, 63–81.
- Pearl, J., Hanel, R., Kunde, V., Maguire, W., Fox, K., Gupta, S., Ponnampereuma, C., Raulin, F., 1979. Identification of gaseous SO<sub>2</sub> and new upper limits for other gases on Io. *Nature* 280, 755–758.
- Pugh, L.A., Narahari Rao, K., 1976. Intensities from infrared spectra. In: Narahari Rao, K. (Ed.), *Molecular Spectroscopy: Modern Research*, vol. 2. Academic Press, New York.
- Rathbun, J.A., Spencer, J.R., Tamppari, L.K., Martin, T.Z., Barnard, L., Travis, L.D., 2004. Mapping of Io's thermal radiation by the Galileo photopolarimeter–radiometer (PPR) instrument. *Icarus* 169, 127–139.
- Retherford, K., 2002. Io's aurora: HST/STIS observations. Dissertation. Department of Physics and Astronomy, The Johns Hopkins University.
- Roesler, F.L., Moos, H.W., Oliverson, R.J., Woodward, R.C., Retherford, K.D., Scherb, F., McGrath, M.A., Smyth, W.H., Feldman, P.D.F., Strobel, D., 1999. Far-ultraviolet imaging spectroscopy of Io's atmosphere with HST/STIS. *Science* 283, 353–357.
- Roldán, C., López-Valverde, M.A., López-Puertas, M., Edwards, D.P., 2000. Non-LTE infrared emissions of CO<sub>2</sub> in the atmosphere of Venus. *Icarus* 147, 11–25.
- Rothman, L.S., Gamache, R.R., Goldman, A., Brown, L.R., Toth, R.A., Pickett, H.M., Poynter, R.L., Flaud, J.-M., Camy-Peyret, C., Barbe, A., Husson, N., Rinsland, C.P., Husson, N., Rinsland, C.P., Smith, M.A.H., 1987. The HITRAN database: 1986 edition. *Appl. Opt.* 26, 4058–4097.
- Rothman, L.S., 30 colleagues, 2003. The HITRAN molecular spectroscopic database: Edition of 2000 including updates through 2001. *J. Quant. Spec. Radiat. Transf.* 82, 5–44.
- Sandford, S.A., Allamandola, L.J., 1993. The condensation and vaporization behavior of ices containing SO<sub>2</sub>, H<sub>2</sub>S, and CO<sub>2</sub>: Implications for Io. *Icarus* 106, 478–488.
- Saur, J., Strobel, D.F., 2004. Relative contributions of sublimation and volcanos to Io's atmosphere inferred from its plasma interaction during solar eclipse. *Icarus* 171, 411–420.
- Saur, J., Neubauer, F.M., Connerney, J.E.P., Zarka, P., Kivelson, M.G., 2004. Plasma interaction of Io with its plasmas torus. In: Bagenal, F., Dowling, T.E., McKinnon, W.B. (Eds.), *Jupiter: The Planet, Satellites, and Magnetosphere*. Cambridge University Press, Cambridge.
- Smith, M.A.H., Rinsland, C.P., Malathy Devi, V., Rothman, L.S., Narahari Rao, K., 1992. Intensities and collision-broadening parameters from infrared spectra: An update. In: Narahari Rao, K., Weber, A. (Eds.), *Spectroscopy of the Earth's Atmosphere and Interstellar Medium*. Academic Press, New York.
- Spencer, J.R., Moore, J.M., 1992. The influence of thermal inertia on temperatures and frost stability on Triton. *Icarus* 99, 261–272.
- Spencer, J.R., Trafton, L.M., Stansberry, J.A., Young, E.F., Binzel, R.P., Croft, S.K., 1997. Volatile transport, seasonal cycles, and atmospheric dynamics on Pluto. In: Stern, A., Tholen, D. (Eds.), *Pluto and Charon*. Univ. of Arizona Press, Tucson, pp. 435–473.
- Spencer, J.R., Jessup, K.L., Yelle, R., Ballester, G.E., McGrath, M.A., 2000a. Discovery of Gaseous S<sub>2</sub> in Io's Pele plume. *Science* 24, 1208–1210.
- Spencer, J.R., Rathbun, J.A., Travis, L.D., Tamppari, L.K., Barnard, L., Martin, T.Z., 2000b. Io's thermal emission from the Galileo photopolarimeter–radiometer. *Science* 288, 1198–1201.
- Strobel, D.F., Wolven, B.C., 2001. The atmosphere of Io: Abundances and sources of sulfur dioxide and atomic hydrogen. *Astrophys. Space Sci.* 277, 271–287.
- Strobel, D.F., Zhu, X., Summers, M.E., 1994. On the vertical thermal structure of Io's atmosphere. *Icarus* 10, 18–30.
- Sumpf, B., 1999. Line intensity and self-broadening investigations in the 19- $\mu$ m band of SO<sub>2</sub>. *Spectrochim. Acta* 55, 1931–1939.
- Trafton, J., Caldwell, J., Barnett, C., Cunningham, C.C., 1996. The gaseous sulfur dioxide abundance over Io's leading and trailing hemispheres: HST spectra of Io's C<sup>1</sup>B<sub>2</sub>–X<sup>1</sup>A<sub>1</sub> band of SO<sub>2</sub> near 2100 Å. *Astrophys. J.* 456, 384. 6-C5.
- Trafton, L.M., Matson, D.L., Stansberry, J.A., 1998. Surface/atmosphere interactions and volatile transport (Triton, Pluto and Io). In: Schmitt, B.,

- de Bergh, C., Feston, M. (Eds.), *Solar System Ices*. In: *Astrophys. Space. Sci. L*, vol. 227. Dordrecht, Kluwer, pp. 773–812.
- Veeder, G.J., Matson, D., Johnson, T., Blaney, D., Gougen, J., 1994. Io's heat flow from infrared radiometry: 1983–1993. *J. Geophys. Res.* 99, 17095–17162.
- Wagman, D.D., 1979. Sublimation pressure and enthalpy of SO<sub>2</sub>. *Chem. Thermodynamics Data Center Natl. Bureau Standards*, Washington, DC.
- Wolven, B.C., Moos, H.W., Retherford, K.D., Feldman, P.D., Strobel, D.F., Smyth, W.H., Roesler, F.L., 2001. Emission profiles of neutral oxygen and sulfur in Io's exospheric corona. *J. Geophys. Res.* 106, 26155–26182.
- Wong, M.C., Johnson, R.E., 1996. A three-dimensional azimuthally symmetric model atmosphere for Io. 1. Photochemistry and the accumulation of a nightside atmosphere. *J. Geophys. Res.* 101, 23243–23260.
- Wong, M.C., Smyth, W.H., 2000. Model calculations for Io's atmosphere at Eastern and Western elongations. *Icarus* 146, 60–74.
- Zhang, J., Goldstein, D.B., Varghese, P.L., Gimelshein, N.E., Gimelshein, S.F., Levin, D.A., 2003. Simulation of gas dynamics and radiation in volcanic plumes on Io. *Icarus* 163, 182–197.